JOURNAL OF GEOPHYSICAL RESEARCH, VOL. 104, NO. D21, PAGES 26,279–26,306, NOVEMBER 20, 1999

Simulated tropospheric NO_x: Its evaluation, global distribution and individual source contributions

H. Levy II and W. J. Moxim

NOAA Geophysical Fluid Dynamics Laboratory, Princeton, New Jersey

A. A. Klonecki

Advanced Studies Program, National Center for Atmospheric Research, Boulder, Colorado

P. S.Kasibhatla

Nicholas School of the Environment, Duke University, Durham, North Carolina

Abstract. Using the 11-level Geophysical Fluid Dynamics Laboratory global chemical transport model, we simulate global tropospheric fields of NO_x, peroxyacetyl nitrate (PAN), HNO_3, and NO_y, as well as the deposition of nitrate, extensively evaluate them against available observations from surface stations and aircraft missions, and quantify the contributions of individual natural and anthropogenic sources. The patterns and magnitudes of simulated and observed HNO_3 wet deposition are generally in good agreement around the globe. Scatterplots of model simulations versus aircraft observations for NO_x and NO_y find ~50% of the points within ±25%, find ~75% within ±50%, and show no systematic global biases. Both simulated and observed vertical profiles have similar shapes with high levels (~1 ppbv or greater) in the polluted boundary layer (BL), very low values in the remote BL, and values increasing from the middle to the upper troposphere. Simulated NO_y, HNO_3, and NO_x + PAN are also in good agreement with extensive lower free tropospheric (FT) observations made at Mauna Loa Observatory. In general, the level of agreement between simulation and observation is as good as the agreement between separate, but simultaneous, observations of NO, NO_x or NO_y. As previous studies have shown, fossil fuel combustion and biomass burning control NO_x levels in most of the lower half of the troposphere with a significant contribution from biogenic emissions. The exceptions are the remote low-NO_x regions where BL and FT sources make comparable contributions. Unlike most previous studies, we find that the much smaller in situ FT sources generally dominate in the upper half of the troposphere. Lightning dominates in the tropics and summertime midlatitudes, and stratospheric injection is the major source in the summer high latitudes. The exception is transported emissions from fossil fuel combustion, which dominate in winter high latitudes. Though seldom dominant, aircraft emissions do have a significant impact on the upper troposphere and lower stratosphere of the northern hemisphere extratropics.

1. Introduction

The oxides of nitrogen are key to our understanding the chemical state of the atmosphere in which we live. NO_x ($NO+NO_2$) is directly, through its role in ozone production [*Chameides and Walker*, 1973; *Crutzen*, 1974], and indirectly, through its impact on OH [*Levy*, 1971], linked to the oxidizing efficiency of the troposphere. A particularly critical NO_x range is 10 - 150 pptv, which depending on the time of year, location in the troposphere, and levels of O_3 and H_2O, determines whether ozone is chemically produced or destroyed in the background troposphere. (See *Fishman et al.* [1979]; *Lin et al.* [1988]; and *Sillman et al.* [1990] for discussions of the dependence of ozone chemistry on NO_x concentration. See *Liu et al.* [1983]; *Chameides et al.* [1987]; *Ridley et al.* [1992]; *Liu et al.* [1992]; and *Jacob et al.* [1996] for discussions of ozone budgets over the remote oceans. See *Klonecki and Levy* [1997] for a discussion of ozone chemical tendencies worldwide.)

Accurate global NO_x fields are a critical component for any realistic simulation of global tropospheric chemistry in general, and tropospheric ozone in particular. With their short tropospheric lifetimes (1-10 days) and numerous diverse and dispersed sources, NO_x mixing ratios range widely from 5 ppbv or more in regions of surface pollution to a few pptv in the marine boundary layer of the remote central Pacific. Currently, NO_x is only sparsely measured throughout the troposphere [e.g., *Emmons et al.*, 1997; *Carroll and Thompson*, 1995]; in the foreseeable future, proposed measurement campaigns will not provide the detailed global time-dependent

Copyright 1999 by the American Geophysical Union.

Paper number 1999JD900442.
0148-0227/99/1999JD900442$09.00

NO_x fields needed to answer a wide range of questions in global tropospheric chemistry. Rather, we will have to rely on simulations by global chemical transport models (GCTM). A minimum requirement for such simulations should be an accurate treatment of the NO_x sources, a realistic representation of the key transport and chemical processes controlling the global distribution of NO_x, and most important, a thorough and critical evaluation of the resulting fields with available observations.

The first comprehensive global nitrogen budget with realistic estimates of the NO_x sources was developed by *Logan* [1983]. *Penner et al.* [1991] published the first simulation of three-dimensional (3-D) global NO_x distributions that attempted to fully capture the complex interactions among transport, chemistry, and geographically inhomogeneous source-sink distributions. However, they did not include the chemistry and transport of peroxyacetyl nitrate (PAN), which has long been thought [*Crutzen*, 1979; *Singh and Hanst*, 1981] and recently has been shown [*Moxim et al.*, 1996] to control NO_x levels in the remote lower troposphere. In this region, O_3 chemistry, which frequently balances between destruction and production, is particularly sensitive to NO_x. Furthermore, their GCTM employed perpetual January and July GCM wind fields and used approximate lightning and biogenic sources that were decoupled from their model's meteorology. They compared their simulated fields with the limited number of NO_x and NO_y measurements then available and concluded that 3-10 TgN/yr was the most likely range for the global lightning source, in harmony with our estimate of 2-6 TgN/yr [*Levy et al.*, 1996].

Dentener and Crutzen [1993] published another simulation which, while the first to include nighttime heterogeneous chemistry, still lacked PAN chemistry and transport and used approximate sources for lightning and soil-biogenic emissions. Moreover, their 10° latitude x 10° longitude GCTM, was driven by monthly mean meteorological fields and did not simulate any synoptic-scale meteorological features, which are fundamentally important elements of tracer transport (see *Levy and Moxim* [1989a,b], *Moxim* [1990], *Moxim et al.* [1996] for some recent examples). While their monthly mean global simulations appear to be qualitatively similar to ours, they present only a limited comparison with actual observations, and we are not able to make a quantitative comparison. In another simulation with monthly mean winds and generic NO_x sources, *Lamarque et al.* [1996] employed a detailed chemistry transported on a 5°x5° grid and reported a global analysis of the NO_x sources. They showed reasonable agreement with observations from Mauna Loa and Niwot, Colorado, and found that lightning plays a dominant role throughout much of the upper troposphere, in agreement with our own study [*Levy et al.*, 1996].

Recently, a number of GCTM simulations employing fully time-varying GCM winds of differing complexity and resolution have been published. *Roelofs and Lelieveld* [1995] reported a global simulation of NO_x but showed no simulated fields and only discussed HNO_3 deposition. Their model had a 5.6°x5.6° horizontal resolution, their lightning and soil-biogenic sources were approximate and decoupled from the model's meteorology, and most important, PAN chemistry and transport were not included. *Kraus et al.* [1996] reported a global NO_x simulation using the 8°x10° version of the Goddard Institute for Space Studies (GISS) GCTM, which assumed a global lightning source of 5 TgN/yr and neglected PAN chemistry. They compared simulated and observed deposition fields over North America, and their simulated monthly mean NO_x values were in qualitative agreement with single flight measurements from the Stratospheric Ozone Experiment (STRATOZ III). *Jaffe et al.* [1997] used the same basic 8°x10° GISS GCTM and similar NO_x sources but carried a very detailed chemistry with 49 reactive species. They performed a more extensive evaluation and found good agreement with surface NO_x observations in source regions, but the model simulations were low in remote regions. A GCTM simulation of reactive nitrogen levels over the North Pacific using NCAR Community Climate Model, version 2 (CCM2) winds (approximately 2.8°x2.8° resolution) and a full chemistry, when compared with measurements from Mauna Loa Observatory (MLO), had reasonable agreement with observed NO_x but 3-8 times the observed levels of HNO_3 and NO_y at Mauna Loa [*Brasseur et al.*, 1996]. *Wang et al.* [1998b] employed the 4°x5° Harvard-GISS GCTM with a comprehensive O_3-NO_x-hydrocarbon chemistry to simulate a wide variety of reactive species. They reproduced NO and PAN within a factor of 2 for a wide range of tropospheric regions but also tended to overestimate HNO_3 in the remote troposphere.

In this study, one of whose primary goals is the production of realistic NO_x fields for the simulation of tropospheric ozone, we employ a GCTM with an effective 2.4°x2.4° resolution in the tropics and 3°-3.5°x2.4° resolution in midlatitudes that is driven by 1 year of time-varying meteorological fields. Three families of tracers (nitrogen oxides, PAN, HNO_3) are transported in the GCTM, and the effective first-order rate coefficients for gas phase and heterogeneous chemical conversions among the families are calculated off-line. The biogenic and lightning emissions are both coupled to the GCTM's meteorology. Without this coupling, the strong episodic emissions of biogenic NO_x are neglected [see *Yienger and Levy*, 1995, Figure 4], and the effective lightning emissions are both underestimated by at least 30% and incorrectly distributed in the vertical [*Levy et al.*, 1996]. After discussing the components of the GCTM in section 2 and the appendix, we evaluate the GCTM's simulations in section 3 by comparing simulated wet deposition and simulated NO_y and NO_x with a wide range of published or released measurements from surface sites, aircraft campaigns, and ship cruises. In section 4 we discuss the 3-D structure of the simulated NO_x distributions and the contributions from individual sources, and in section 5 we discuss potential sources of error in the simulations and their possible impacts on our conclusions.

2. GCTM Description

With a horizontal grid size of ~265 km, our GCTM has an effective horizontal resolution of 2.4°x2.4° in the tropics and 3°-3.5°x2.4° in midlatitudes and captures large-scale transport due to extratropical cyclones and synoptic meteorology in general [e.g., *Moxim*, 1990; *Moxim et al.*, 1996]. Its 11 vertical levels with standard pressures and (thicknesses) of 990 mbar (1000 - 981), 940 mbar (981 - 902), 835 mbar (902 - 773), 685 mbar (773 - 607), 500 mbar (607 - 412), 315 mbar (412 - 241), 190 mbar (241 - 150), 110 mbar (150 - 81), 65 mbar (81 - 52), 38 mbar (52 - 27), and 10 mbar (27 - 0) provide three levels for the boundary layer (BL) (990, 940, 835 mbar), three to four levels (685, 500, 315, 190 mbar) for the free troposphere (FT), and coarser resolution of the tropo-

pause region and the stratosphere. The GCTM is driven by 12 months of 6-hour time-averaged wind, temperature, and precipitation fields from an earlier Geophysical Fluid Dynamics Laboratory (GFDL) general circulation model (GCM) with no diurnal insolation (see *Mahlman and Moxim* [1978] for details of the GCTM's transport module, and *Manabe et al.* [1974] and *Manabe and Holloway* [1975] for details of the parent GCM).

We explicitly separate reactive nitrogen (NO_y) into three classes of transported species: nitrogen oxides ($NO+NO_2+NO_3+N_2O_5$), HNO_3, and PAN. HNO_3 is a surrogate for all soluble inorganic nitrogen, and PAN is a surrogate for all organic nitrates. Although the HNO_4 reservoir species is implicitly included in our simulation of upper tropospheric HNO_3, it does not explicitly interact with NO_x.The physical sinks for the chemical tracers are dry deposition of NO_x and PAN over land; dry deposition of HNO_3 over land, oceans, ice, and snow; and deposition of HNO_3 in precipitation.

Effective first-order rate coefficients for the daytime chemical interconversions among NO_x, HNO_3, and PAN are interpolated from monthly mean, zonally averaged tables carried in the GCTM. These are precalculated for specified monthly mean fields of NO_x, CO, CH_4, nonmethane hydrocarbon (NMHC), O_3, H_2O, temperature, and pressure using a standard O_3-CO-CH_4-NO_x-H_xO_y chemical scheme [e.g., *Chameides and Tan,* 1981]. These interpolation tables, which represent a significant simplification of the full in situ chemistry, were initially developed for individual NO_x source studies by *Kasibhatla et al.* [1991, 1993] and focus on predicting realistic OH levels and NO:NO_2 ratios. The nighttime first-order rate coefficients for heterogeneous conversion of NO_2 to HNO_3 on sulfate aerosol via NO_3 and N_2O_5 are calculated off-line and carried as monthly average 3-D fields.

Our present global NO_x sources include fossil fuel combustion (22.4 TgN/yr), biomass burning (7.8 TgN/yr), and soil-biogenic emissions (5.0 TgN/yr) in the BL [*Levy and Moxim,* 1989a,b; *Benkovitz et al.*, 1996; *van Aardenne et al.*, 1999; *Levy et al.*, 1991; M.K. Galanter et al., Impacts of biomass burning on tropospheric CO, NO_x, and O_3, submitted to *Journal of Geophysical Research*, 1999 (hereinafter referred to as submitted paper); *Yienger and Levy*, 1995] and lightning discharge (4.0 TgN/yr), aircraft emissions ([0.45TgN/yr), and stratospheric injection (0.64TgN/yr) in the FT [*Levy et al.*, 1996; *Kasibhatla et al.*, 1991; *Kasibhatla*, 1993]. The annual zonally integrated sum of all sources of NO_x is plotted as a function of latitude and shown as the shaded area in Figure 1. The total NO_x source is dominated by BL emissions whose contribution is represented by the dashed line. Both the total source and the BL contribution are concentrated in the northern midlatitudes and are primarily from fossil fuel emissions in the continental-scale metro-agro-plexes [*Chameides et al.*, 1994], while biomass burning and soil-biogenic emissions contribute in the tropical BL. NO_x emissions in the FT, ~12% of the total (solid line in Figure 1), are primarily from lightning and found over the tropics and over midlatitude continents in summer. Small contributions are provided by stratospheric injection in the high latitudes of both hemispheres and by aircraft in the midlatitudes and high latitudes of the northern hemisphere (NH).

Detailed discussions of the GCTM's treatment of resolved advection, its subgrid-scale parameterizations of horizontal and vertical transport by turbulence and convection, its parameterizations of wet and dry deposition, its daytime gas phase and nighttime heterogeneous chemistry, and its six NO_x sources are provided in the appendix.

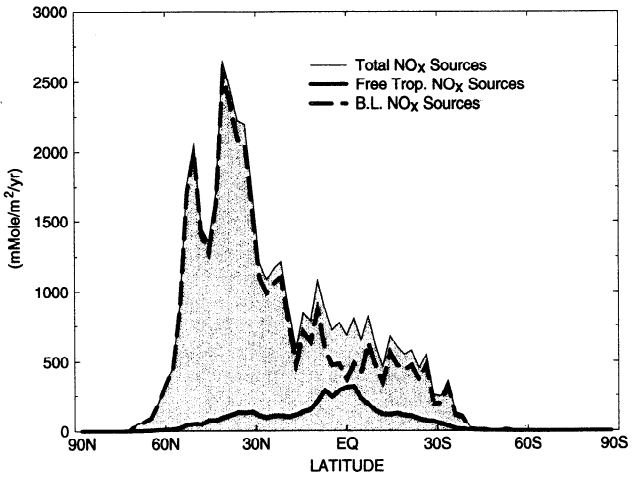

Figure 1. The zonal integral of the total column NO_x source (mmol/m^2/yr) is given by the shaded area, while the zonal integral of the BL NO_x sources (mmol/m^2/yr) is given by the dashed line and the zonal integral of the FT NO_x sources (mmol/m^2/yr) is given by the solid line.

3. GCTM Evaluation

Before examining the simulated NO_x global distributions and the relative roles of individual sources, we evaluate the GCTM's performance by comparing its NO_x, NO_y, and HNO_3 simulations with a variety of observations that test different aspects of the complex interactions among transport, chemistry, deposition, and sources in the GCTM. We have already evaluated the PAN portion of this study in an earlier paper [*Moxim et al.*, 1996]. Since the GCTM is driven by a single year of simulated meteorology, rather than the weather for a particular observation period in a given year, it would be best to compare the simulated fields with multiyear observations when possible. Failing that, we focus on measurement campaigns (e.g., MLO Photochemistry Experiment (MLOPEX), Atmospheric Boundary Layer Experiment (ABLE), Pacific Exploratory Mission (PEM-West A and B, and PEM-Tropics A) and Transport and Atmospheric Chemistry Near the Equator-Atlantic (TRACE-A)) that give multiflight coverage of a region for a season and compare the observations with model data that have been completely sampled for the same season and region. When comparing a 1 year simulation with an observed climatology, there is always the possibility that the 1 year of simulated weather is not representative of a particular region's climatology. This problem becomes even worse when there is only a single season of observations, since neither observations nor simulations may be representative of the region's climatology. While some ship cruise and single flight track observations (e.g., STRATOZ) are also included in this evaluation, their comparison with a GCTM simulation may be problematic.

There are also a number of measurement issues. The possibility of significant measurement error in observed gas phase concentrations, particularly the NO_2 and NO_y observations from aircraft [e.g., *Crawford et al.*, 1996; *Crosley*, 1996; *Bradshaw et al.*, 1998], is of primary concern. The regional

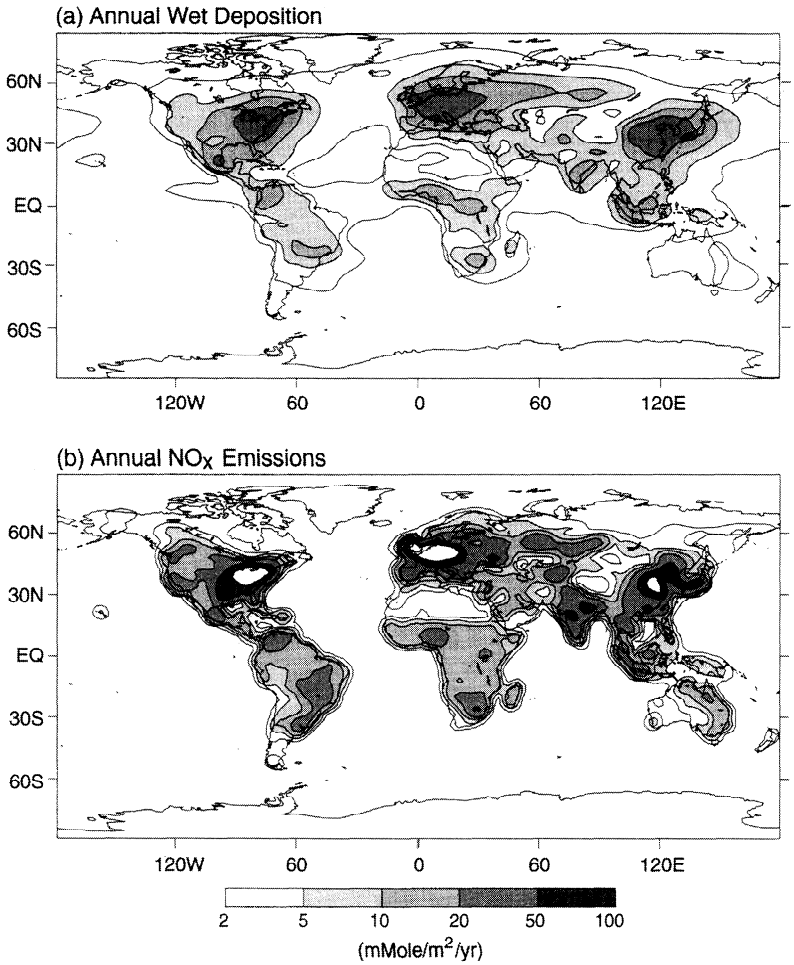

Figure 2. (a) Global map of the simulated annual column integral of nitrate wet deposition (mmol/m^2/yr) for the present level of emissions and (b) a global map of the annual column integral of present NO_x emissions (mmol/m^2/yr).

and temporal representativeness of the sparse data sets from aircraft and the regional representativeness of some of the wet deposition samplers and other surface measurements, which may be significantly skewed by local emissions, meteorology, and topography, also introduce uncertainty. Therefore, while we would certainly prefer that the simulations and observations agree quantitatively, it is critical that they display similar patterns regarding the expected large variations with season, height, and region.

3.1. HNO_3 Deposition

In the BL source regions, wet and dry deposition are comparable, and the patterns of deposition and emission should be highly correlated. This is demonstrated by Figures 2a and 2b, annual global maps of simulated wet deposition of nitrate and the GCTM's column integrated NO_x source. Note that the white inside black areas represents emissions greater than 100 mmol/m^2/s. Therefore a comparison of observed and simulated deposition patterns and magnitudes in source regions will provide an evaluation of both the spatial distribution and the absolute magnitude of the surface NO_x sources used in the GCTM. While some local comparisons of HNO_3 wet deposition may be affected by local precipitation differences between the model's 1 year of weather and the actual climatology at a particular observation site as well as any local anomalies in observed precipitation, the overall patterns of the observed and simulated wet deposition in the source region should correlate strongly if the GCTM's BL sources are realistic. In more remote regions, comparisons of simulated and observed wet deposition will evaluate a combination of the model's wet deposition, its HNO_3 formation rate, and its simulated long-range transport.

In Figure 3a we have binned multiyear annual wet deposition observations from 236 National Acid Deposition Program (NADP) collection sites around the United States [*NADP/NTN*, 1998; J. Sulzman, private communication, 1998] into 121 model grid boxes and plotted them against simulated wet deposition. While simulation and observation are highly correlated, the simulated wet deposition is systematically high by 20-25%. This is confirmed by a least squares linear regression of all 121 points that gives a correlation coefficient of 0.87 with a slope of 1.28 for a 0.0 offset and a slope of 1.18 for a 1.7 mmol/m^2/yr offset. The missing of very small precipitation events by the NADP automatic lid system may support a small offset but should not be large enough to support a 20-25% systematic error. Centered about the +25% line, 40% of the points fall between +50% and 0.0, 75% fall within +75% and -25%, and only ~12% are significant outliers.

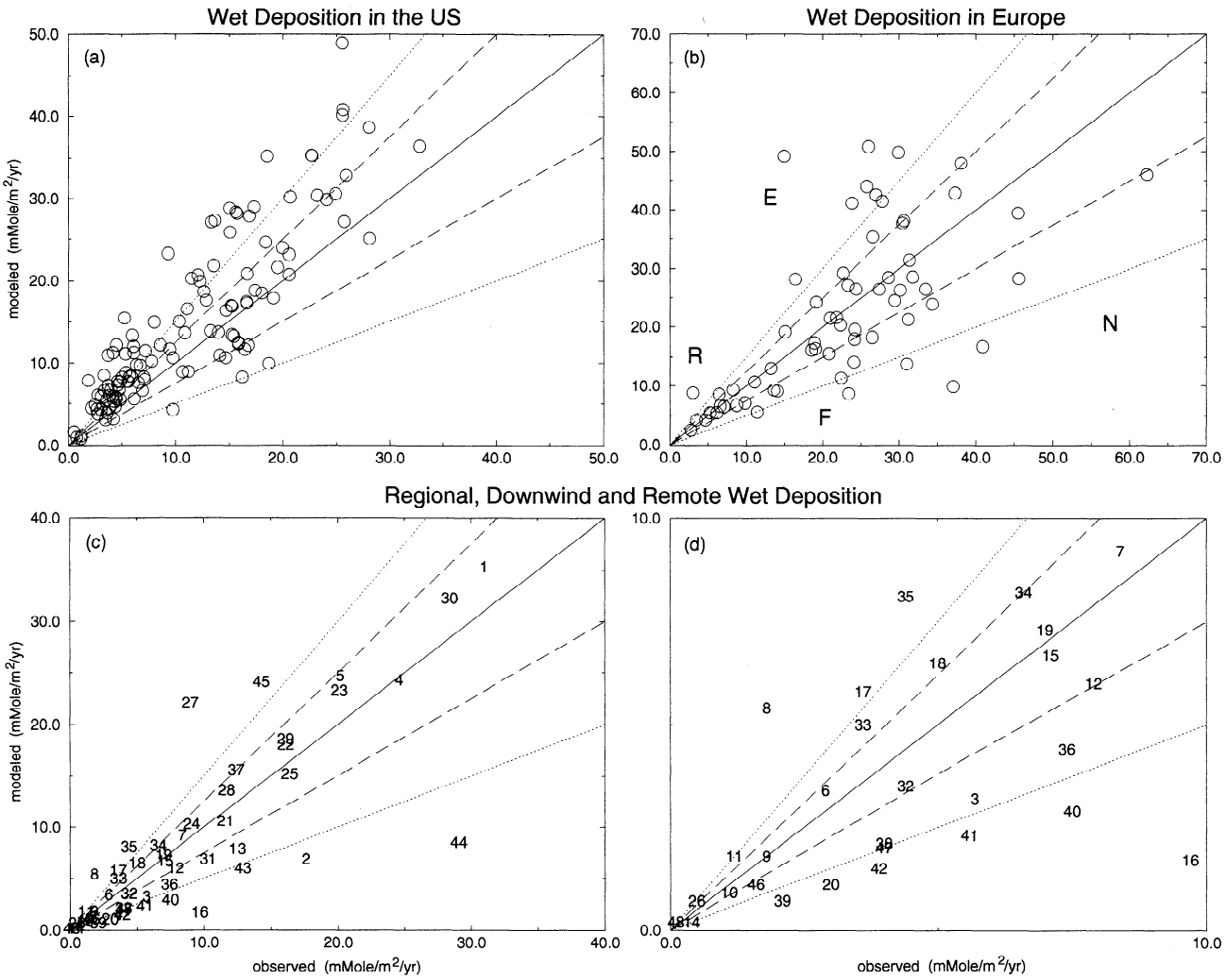

Figure 3. Comparisons of simulated annual wet deposition of nitrate (mmol/m^2/yr) with (a) multiyear annual wet deposition observations from 236 NADP collection sites around the United States binned into 121 GCTM grid boxes; (b) multiyear annual wet deposition observations from 108 EMEP sites throughout Europe binned into 67 GCTM grid boxes; (c) annual wet deposition observations from 48 sites around the world: 1, Harvard Forest; 2, Faroe Island; 3, Norway; 4, Sweden; 5, Baltic Sea; 6, N. Atlantic; 7, Ireland; 8, Portugal; 9, Amsterdam Is.; 10, Samoa; 11, Hawaii; 12, Amazon Basin; 13, San Carlos Vez.; 14, Torres de Paine; 15, Lake Calado, Brazil; 16, Puerto Rico; 17, Costa Rica; 18, central Amazonia; 19, Bermuda; 20, Barbados; 21, south Florida; 22, Nova Scotia; 23, New Brunswick; 24, Newfoundland; 25, Quebec; 26, Poker Flats, Alaska; 27, Beijing, China; 28, Guizhou China; 29, Hong Kong; 30, Linan China; 31, Allabahad, India; 32, Jodphur, India; 33, Minicoy Island; 34, Nagpur, India; 35, Pune, India; 36, Port Blair, India; 37, Ryori, Japan; 38, Katherine, Australia; 39, Cape Grim, Tazmania; 40, N. Australia; 41, Wagga Wagga, Australia; 42, New Plymouth, New Zealand; 43, S. Congo; 44, N. Congo; 45, Nigeria; 46, Cape Point, South Africa; 47, Dye 3, Greenland; 48, South Pole. Figure 3d is the same as Figure 3c except it is only for those observations in the range 0.0-10.0 mmol/m^2/yr. The solid line represents 1:1, the large dashes represent 1.25:1 and 1:1.25, and the short dashes represent 1.5:1 and 1:1.5.

In Figure 3b we have binned multiyear annual wet deposition observations from 108 European Monitoring and Evaluation Programme (EMEP) sites throughout Europe [*Hjellbrekke et al.*, 1996] into 67 model grid boxes and plotted them against simulated values. Although there is more scatter than in Figure 6a, they are well correlated and show no systematic bias. Centering about the 1:1 line, we find 50% of the points within ±25%, 75% within ±50%, and ~10% remaining as significant outliers. Particularly anomalous examples are the Faroe Island site in the remote North Atlantic (labeled "F" in Figure 3b) which reports 20 mmol/m^2/yr; an English midlands industrial site (labeled E) with only 13 mmol/m^2/yr, and another site from the Russian/Finnish border (labeled R) with only 3 mmol/m^2/yr; and a southern coastal site in Norway (labeled N) with over 200 cm/yr of precipitation which reports one of the highest depositions in our EMEP data set (57.5 mmol/m^2/yr). After trimming the most extreme outliers (5%), a least squares regression gives a slope of 0.95 with a correlation coefficient of 0.75.

In Figure 3c, annual wet deposition observations from 48

sites around the world employing a wide range of collection techniques are plotted against the GCTM simulation. The sites provide observations from African, Asian, and South American BL source regions, regional and coastal sites downwind of major source regions, and remote maritime sites (see *Levy and Moxim* [1989a,b], *Kasibhatla et al.* [1993], and *Dentener and Crutzen* [1994] for specific references). A least squares fit of the 48 points gives a slope of 0.95 with a correlation coefficient of 0.83. Centered about the 1:1 line, we find 40% of the points falling within ±25% and 70% within ±50% with 10 significant outliers. The agreement between simulation and observation for the regional and coastal sites downwind of major source regions is generally quite good, as a correlation coefficient of 0.83 would suggest. While the North Congo site (44) is an extreme outlier with very high observed wet deposition (30 mmol/m^2/yr) that exceeds most NADP and EMEP observations, the South Congo site (43) is reasonable, and recent rainy season measurements from the Sahelian savanna of Niger (~6 mmol/m^2/yr [*Lacaux and Modi*, 1998]) are in agreement with the GCTM. Figures 3a - 3c, along with the associated correlation coefficients, demonstrate that the GCTM's HNO_3 wet deposition, with the exception of outliers that may be due to either anomalous local observations or local errors in the GCTM's NO_x source and simulated precipitation, captures the observed spatial patterns and magnitudes of wet deposition in the BL source regions. Therefore we argue that both the magnitude and spatial distribution of the GCTM's NO_x BL sources are generally realistic.

In Figure 3d, we examine the low deposition sites (< 10 mmol/m^2/yr) from Figure 3c. The simulated deposition at many of the most remote sites is systematically low, as it is for Puerto Rico, the three Australian sites, Cape Grim, and New Zealand. While precipitation discrepancies are part of the problem, we currently do not have an explanation for the GCTM's apparent systematic underestimate of observed wet deposition in the Australia-New Zealand region. Modeled dry deposition cannot explain the discrepancies, since it is a small fraction of total deposition at remote sites. In a further evaluation of the long-range transport of HNO_3, which is not presented in a table or figure, simulated surface levels of HNO_3 are compared with measured soluble nitrogen at a number of remote island sites. While there is reasonable agreement at Shemya, Midway, New Caledonia, and Norfolk in the Pacific, we simulate approximately 1/2 the levels measured at Bermuda and Barbados in the Atlantic and at Enewetak, Fanning, Nauru, Funafutti, Samoa, and Rarotonga in the remote tropical Pacific [*Savoie et al.*, 1989; D. L. Savoie, private communication, 1995]. This suggests a number of possibilities: local sources of soluble nitrogen in the remote oceans, deficiencies in the wet deposition parameterizations, and deficiencies in the simulated long-range transport of HNO_3 and/or NO_x and PAN.

To assess the impact of possible deficiencies in the GCTM's treatment of wet deposition, we impose a 50% global reduction in the model's effective first-order precipitation removal coefficient. This does remove the 20-25% positive bias in the U.S. nitrate deposition, bring Bermuda and Barbados into agreement for surface levels of soluble nitrogen, and significantly improve the comparison in the remote tropical Pacific. However, it also introduces a negative bias of 15-20% for nitrate deposition in Europe, elevates free tropospheric HNO_3 and NO_y levels significantly above those observed, and simulates nearly double the level of HNO_3 observed at Mauna Loa Observatory during the MLOPEX campaign. Fortunately, as *Kasibhatla et al.* [1993] already found for fossil fuel sources, we also find that NO_x levels in both source regions and the free troposphere are relatively insensitive to uncertainties in the rate coefficient for precipitation removal when all NO_x sources are considered.

3.2. Gas Phase Measurements

A number of campaigns, primarily aircraft, have measured reactive trace gases around the world. This reasonably extensive set of observations in the free troposphere and remote boundary layer, as well a small data set from the continental source region, will be used to evaluate the GCTM's simulation of the complex interactions among NO_x sources, resolved and subgrid-scale transport, chemical interconversion and physical removal that all combine to produce the global NO_x fields. Most of the available data have recently been collected, organized, and summarized by *Emmons et al.* [1997]. We have gathered the aircraft-based data from the compilation of *Emmons et al.* [1997], the Georgia Tech merged data sets, and the NCAR New Mexico campaign and subdivided the 12 measurement campaigns into 29 regions based on common meteorological and source characteristics. These 29 regions are listed in Table 1 and shown in Figure 4. While not identical to those selected by *Emmons et al.* [1997], the basic reasoning is similar. We then determine means, medians, and related statistics for all the observations from the equivalent model layers in a given region and calculate the means, medians, and related statistics for all the simulated data in each model level of the same region over the full period of each measurement campaign. For each model level in each measurement region, we analyze a complete sample from the GCTM fields and compare it with a spatially and temporally sparse sample of observations.

3.2.1. Aircraft NO_y comparisons. NO_y, the sum of reactive oxidized nitrogen compounds, has a multiday lifetime controlled by wet and dry deposition. It acts as a relatively conserved transport tracer, particularly in the upper troposphere, where precipitation removal is much less active. Direct tropospheric measurements of NO_y from aircraft, which comprise the bulk of the available data in the free troposphere, have serious problems [*Crosley*, 1996], and most measurements have now been withdrawn for further analysis (J. Bradshaw, private communication, 1997; S. T. Sandholm, private communication, 1998). Therefore, in Figure 5 we compare our simulated NO_y with the sum of the individual measurements of NO_x, HNO_3, and PAN. Both observations and simulations are assembled, as described above, for the model's tropospheric layers (190 (30°N - 30°S), 315, 500, 685, 835, 940, 990 mbar).

Half of the total comparisons fall within ±25% of each other, and 70-80% fall within ±50%, with most of the significant outliers occurring in regions 16, 17, 23, and 25, where simulations significantly exceed observations. In general, the model simulates a realistic global distribution of NO_y, though FT NO_y, particularly HNO_3, over the western North Pacific in spring and fall is frequently higher than observed. This high bias is most noticeable in the middle and upper troposphere, where the GCTM's implicit inclusion of HNO_4, which was not measured, is only part of the explanation. It cannot account for the late winter and early spring measurements over the Sea of Japan and in the vicinity of Japan (315 - 685 mbar

Table 1. Aircraft Measurement Regions

Region	Campaign	Longitude, deg	Latitude, deg	Month	Reference
1	AASE	0-10E	58N-63N	Jan.-Feb.	1
2	ABLE 2A	70W-45W	8S-2N	July-Aug.	2
3	ABLE 2B	65W-45W	6S-EQ	April-May	3
4	ABLE 3A	175W-105W	50N-80N	July-Aug.	4
5	ABLE 3B	72W-52W	45N-65N	July-Aug.	5
6	ABLE 3B	95W-77W	45N-65N	July-Aug.	5
7	CITE 2	125W-110W	35N-40N	Aug.-Sept.	6
8	CITE 2	130W-125W	30N-45N	Aug.-Sept.	6
9	CITE 3	35W-26W	11S-3N	Aug.-Sept.	7
10	CITE 3	77W-69W	31N-41N	Aug.-Sept.	7
11	New Mexico	108W	33N	Aug.-Aug.	8
12	PEM-Tropics A	170E-160W	50S-EQ	Aug.	9
13	PEM-Tropics A	171E-173E	73S-45S	Aug.	9
14	PEM-Tropics A	111W-109W	50S-28S	Aug.	9
15	PEM-Tropics A	160W-120W	25S-EQ	Aug.	9
16	PEM-West A	110E-140E	EQ-30N	Sept.-Oct.	10
17	PEM-West A	110E-155E	30N-40N	Sept.-Oct.	10
18	PEM-West A	140E-180E	EQ-20N	Sept.-Oct.	10
19	PEM-West A	160E-130W	45N-55N	Sept.-Oct.	10
20	PEM-West A	180W-140W	10N-30N	Sept.-Oct.	10
21	PEM-West A	140W-120W	25N-35N	Sept.-Oct.	10
22	PEM-West B	110E-140E	EQ-30N	Feb.-March	11
23	PEM-West B	110E-155E	30N-40N	Feb.-March	11
24	PEM-West B	140E-180E	EQ-20N	Feb.-March	11
25	PEM-West B	160E-130W	45N-55N	Feb.-March	11
26	PEM-West B	180W-140W	10N-30N	Feb.-March	11
27	TRACE-A	12E-40E	35S-10S	Sept.-Oct.	12
28	TRACE-A	20W-10E	20S-EQ	Sept.-Oct.	12
29	TRACE-A	55W-35W	30S-5S	Sept.-Oct.	12

1, *Carroll et al.* [1990]; 2, *Harriss et al.* [1988]; 3, *Harriss et al.* [1990]; 4, *Harriss et al.* [1992]; 5, *Harriss et al.* [1994]; 6, *Hoell et al.* [1990]; 7, *Hoell et al.* [1993]; 8, *Ridley et al.* [1994]; 9, *Hoell et al.* [1999]; 10, *Hoell et al.* [1996]; 11, *Hoel et al.* [1997]; 12, *Fishman et al.* [1996]. AASE, Airborne Arctic Stratospheric Experiment; ABLE, Arctic Boundary Layer Expedition; CITE, Chemical Instrumentation Test and Evaluation; PEM, Pacific Exploratory Mission; TRACE-A, Transport and Atmospheric Chemistry Near the Equator-Atlantic.

in region 23) being so much lower than those simulated by the GCTM, where both fossil fuel emissions from the Asian BL and in situ aircraft emissions appear to dominate (see Figure 9a and Plate 1). Although it is possible that individual flights sampled air in which HNO_3 had recently been removed, it is unlikely that this would have happened for all flights, and we have the same bias in the NO_x data (see Figure 6). The model's seasonal circulation in that region is in excellent agreement with observed climatology. It is possible that either the GCTM mixed too large a fraction of the surface emissions into the free troposphere during early March around Japan or the actual BL mixing was greatly suppressed in early March. It does not appear from the PEM-West B meteorological analysis [*Merrill et al.*, 1997] that there was more northwest transport of relatively clean air from the Arctic during the early March measurement period than would be expected from the mean circulation of either the observed climatology or the GCTM. The simulated time series in region 23 do have some low background values, which are in reasonable agreement with the observations, but they also have a number of pollution events which greatly elevate both the simulated mean and median values. At this time, we do not have a full explanation for the GCTM's apparent systematic high bias in region 23.

3.2.2. Tropospheric NO_x comparisons. The highly variable tropospheric NO_x fields, which are the key to the production of O_3 throughout most of the troposphere, are the primary focus of this study. Current analyses finds that measurements of NO from aircraft are relatively reliable, though it is worth noting that a side-by-side intercomparison of two NO measurement devices during PEM-West A found only ~50% of the comparisons falling within ±25% for NO < 50 pptv [see *Crosley*, 1996]. While upper tropospheric measurements of NO_2 frequently exceeded in situ steady state calculations by a factor of 2 or more during PEM-West A and B and TRACE-A [e.g., *Crawford et al.*, 1996], PEM-Tropics A measurements and in situ steady state calculations were in reasonable agreement [*Bradshaw et al.*, 1999]. Although NO measurements are more reliable, NO's very short chemical lifetime leads to rapid fluctuations driven by local changes in the environment. Between the extremely high observed standard deviations and simulated NO values only being available as daytime averages, useful NO comparisons are not possible. Therefore we compare simulated NO_x with observed NO + calculated NO_2 for PEM-West B and observed NO + observed NO_2 for the rest. A single NO_x observation for a particular level and region is the mean of 1-3 minute measurements from any flight that was contained in that level and region. It is not likely that all the observations are meteorologically independent, nor is it likely that they represent an unbiased sample and a true climatology. However, the evaluation regions were selected to minimize meteorological inhomogeneity, and they do represent the most complete global set of NO_x observations available.

Comparisons of simulated and observed median values of NO_x for the free troposphere and the relatively unpolluted boundary layer are presented as scatterplots in Figure 6. At each level, we include an observed median from every region

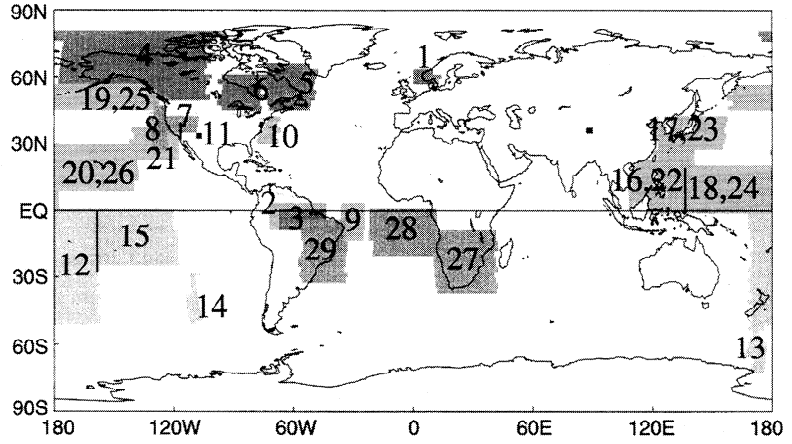

Figure 4. Locations of the 29 regions (see Table 1 for a detailed description) selected from the 12 aircraft-based measurement campaigns.

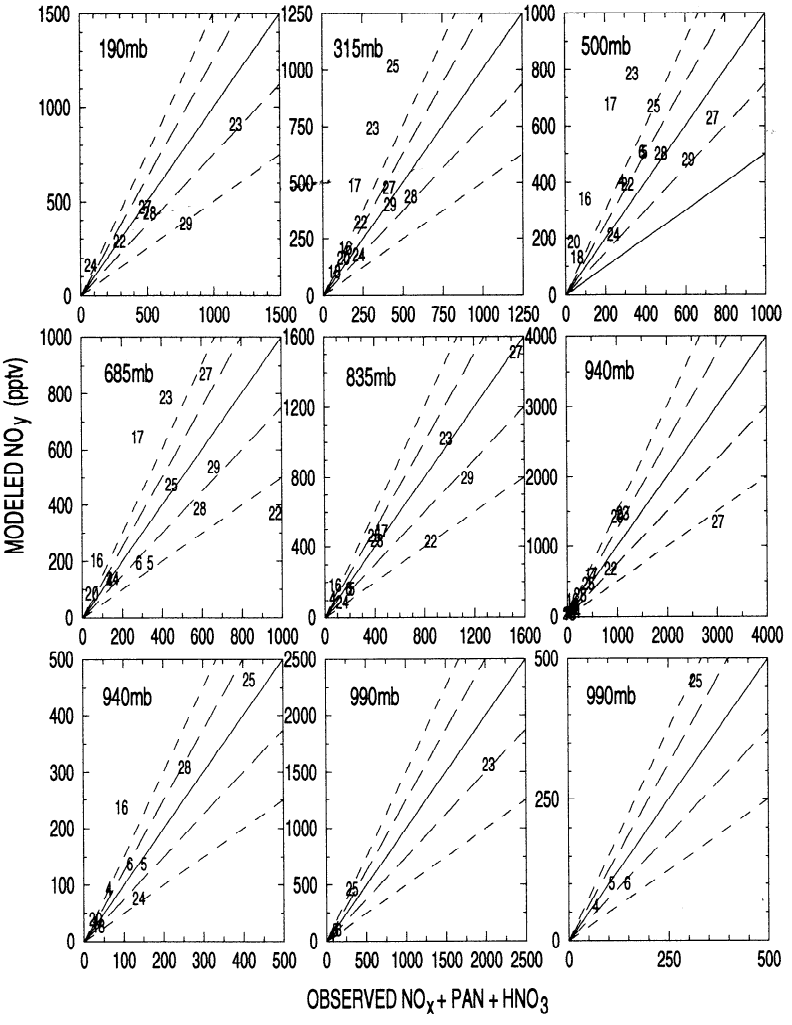

Figure 5. Comparisons of simulated NO_y medians with the medians of the sums of observed NO_x + observed HNO_3 + observed PAN for the GCTM's seven tropospheric levels in the 29 regions listed in Table 1. A comparison is only made if there are at least six observations from a given level of a particular region. The numbers represent individual regions that are pictured in Figure 4. Note that panels with expanded scales have been provided for 940 and 990 mbar. The solid line represents 1:1, the large dashes represent 1.25:1 and 1:1.25, and the short dashes represent 1.5:1 and 1:1.5.

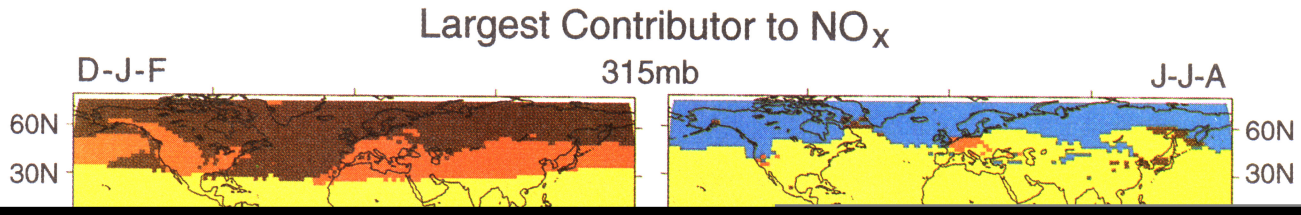
Largest Contributor to NOx
D-J-F
315mb
J-J-A
60N
30N
60N
30N

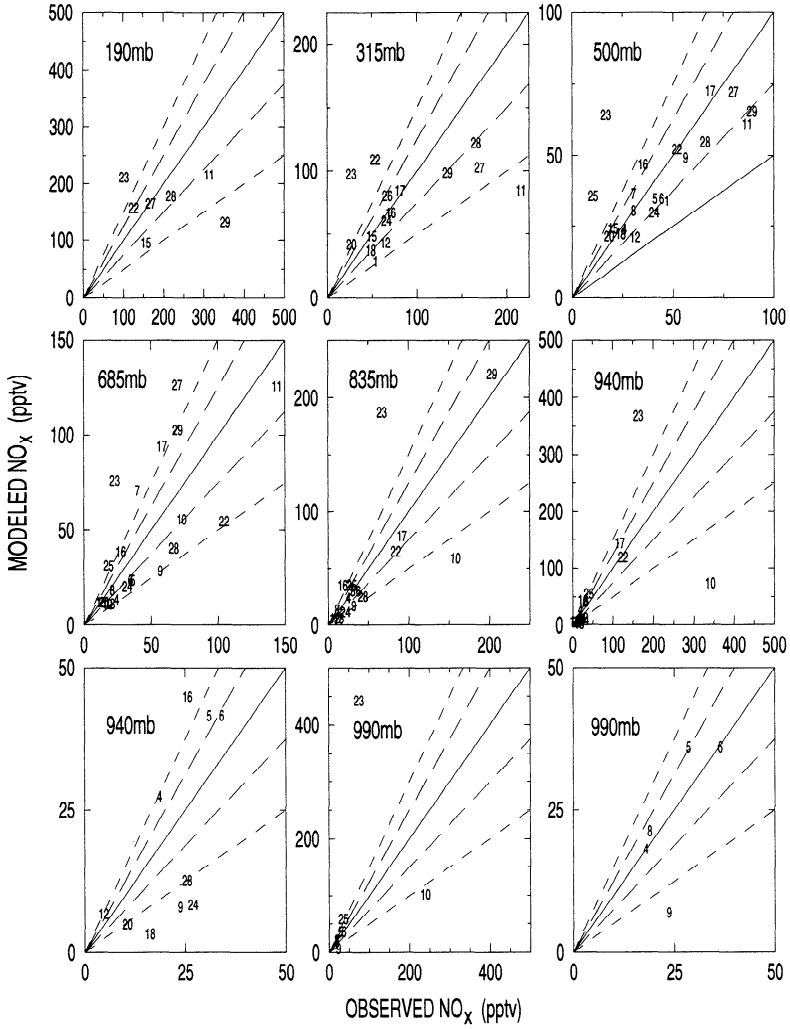

Figure 6. Comparisons of simulated NO_x medians with either observed NO_x medians or observed NO medians + calculated NO_2 medians for the GCTM's seven tropospheric levels in the 29 regions. A comparison is only made if there are at least six observations from a given level of a particular region. The numbers represent individual regions that are described in Table 1 and pictured in Figure 4. Note that panels with expanded scales have been provided for 940 and 990 mbar. The solid line represents 1:1, the large dashes represent 1.25:1 and 1:1.25, and the short dashes represents 1.5:1 and 1:1.5.

(see Figure 4) with at least six observations. With the exception of regions 10 and 23, there are no apparent systematic biases in the simulated NO_x. Of the 102 comparisons, 75% fall within ±50% of the 1:1 line and 44% within ±25% of the line. There are 15 significant outliers, 11 of which are from regions 23 and 10. The low observations from region 23 were already noted in section 3.2.1. Region 10, with relatively high observations, is a summertime Chemical Instrumentation Test and Evaluation-3 (CITE-3) campaign off the East Coast of the United States. The GCTM summertime circulation establishes a strong Bermuda High, which prevents the transport of simulated U.S. pollution during late July and August, while the actual circulation, which does establish a strong Bermuda High during some summers, did not do so during the CITE-3 measurement period.

In Figure 7 we show plots of vertical profiles from the 14 regions with complete vertical soundings. The GCTM captures the basic tropospheric vertical profiles for a wide range of regions, and there is a strong overlap between the middle 50% or interquartile ranges (IQR) of the observations and the simulations. Even in region 23, both profiles have the same shape. Over or near source regions (e.g., 11, 16, 27, or 29), there is a clear midtropospheric minimum, while over remote regions (e.g., 12, 15, 18, 24, or 28), both observed and simulated have a minimum in the BL and increase with height.

In Table 2 we compare simulated and observed NO_x median values, as well as IQRs, from a variety of surface locations, primarily in North America. With surface NO_x values having a large diurnal variation in source regions, daytime measurements are most representative of a well-mixed boundary layer value. Therefore we compare these daytime observations with daily average simulations from the GCTM boundary layer (990, 940, and 835 mbar), which has no diurnal variability. These BL values are mass-weighted averages from the three lowest model levels, with each level weighted by the fraction of BL mass that it contains. At remote and nonsource sites where the observed diurnal variation is much less, we compare daily-averaged surface observations of NO_x with daily averages from the GCTM lowest level (990 mbar). While the GCTM summertime medians in the source region are system-

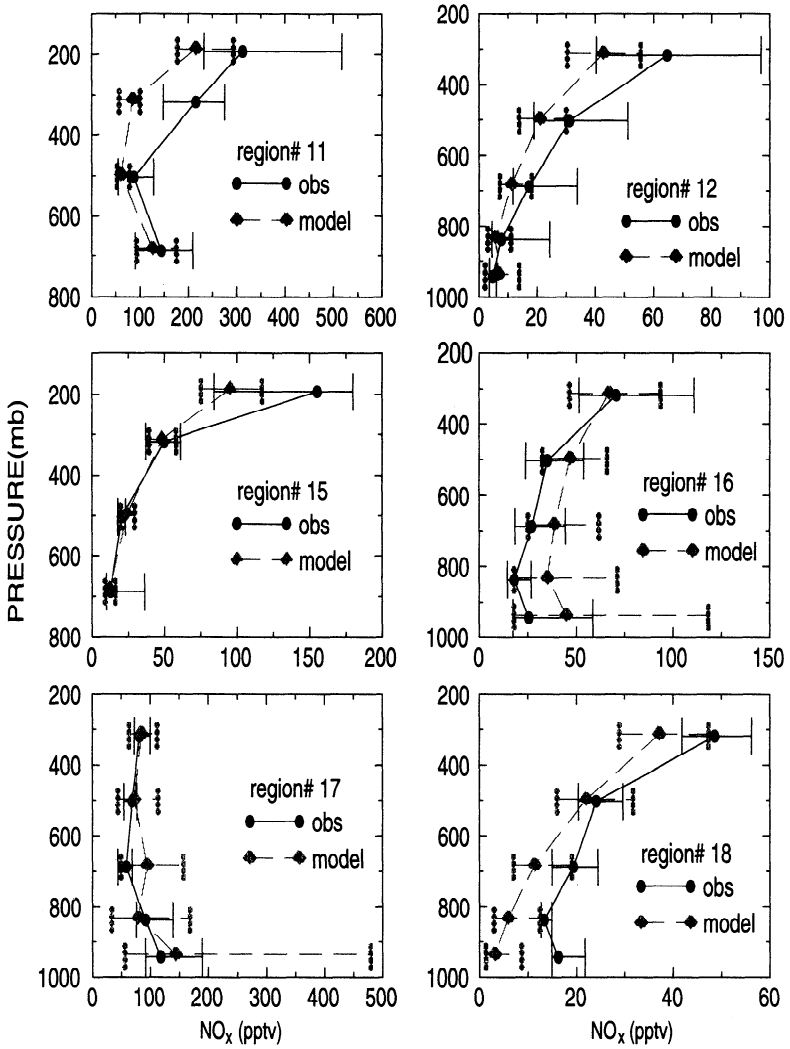

Figure 7. Vertical profiles of simulated and observed NO_x median values, with their interquartile ranges (IQR) represented by brackets, are displayed for those 14 regions with sufficient data. The observed medians are represented by solid circles, and the GCTM medians by solid diamonds. The horizontal brackets represent the respective IQRs.

atically higher than observed, it seems reasonable that a 265 km x 265 km grid box with well-mixed local sources would have a higher background than rural observations, and the respective IQRs do have a large overlap. The simulated surface values at Sable Island are in excellent agreement with observations, and both observations and simulations are very low over the remote ocean. The NO_x levels observed on the Atlantic Stratocumulus Transition Experiment (ASTEX) cruise are higher than those simulated. However, the NO_2 instrument was operating near or at its detection limit (T. P. Carsey and R. Dickerson, private communications, 1998), and the reported measurements may not be significantly different from 0.0. Summertime 1990 aircraft measurements of lower tropospheric NO_x over southern Alabama [*Ridley et al.*, 1998] are at least a factor of 2 lower than the simulation. We believe this is due to a GCTM transport deficiency, which results in insufficient ventilation by relatively clean/moist air from the Gulf of Mexico, and is apparently related to the parent GCM's precipitation deficiency along the Gulf Coast.

3.2.3. Mauna Loa Observatory data. The bulk of reactive nitrogen observations were either taken from aircraft, thereby providing a very sparse sample of the free troposphere, or were taken from the highly variable and complex surface layer and were quite difficult to interpret. However, the MLOPEX data set, when filtered to exclude surface air, provides 6 week samples of the lower free troposphere from the MLO for all four seasons. While even this relatively simple system shows some inconsistencies between observed and calculated species, suggesting some combination of measurement error and missing chemistry [e.g., *Hauglustaine et al.*, 1996a], it remains a relatively complete and consistent data set from the remote lower free troposphere. It should provide a useful check on the model's treatment of transport and reactive nitrogen chemistry in that region.

In Table 3 we compare NO_y, HNO_3, PAN, and NO_x medians and IQRs from the GCTM 685 mbar layer with observations that have been filtered to only include downslope conditions [*Atlas and Ridley*, 1996; NCAR/MLOPEX Data Archive]. It is apparent that measured NO_y greatly exceeds the sum of the three major measured species. Either there was an important reactive nitrogen species not measured at MLO, or the NO_y measurement includes a major artifact. On the oth-

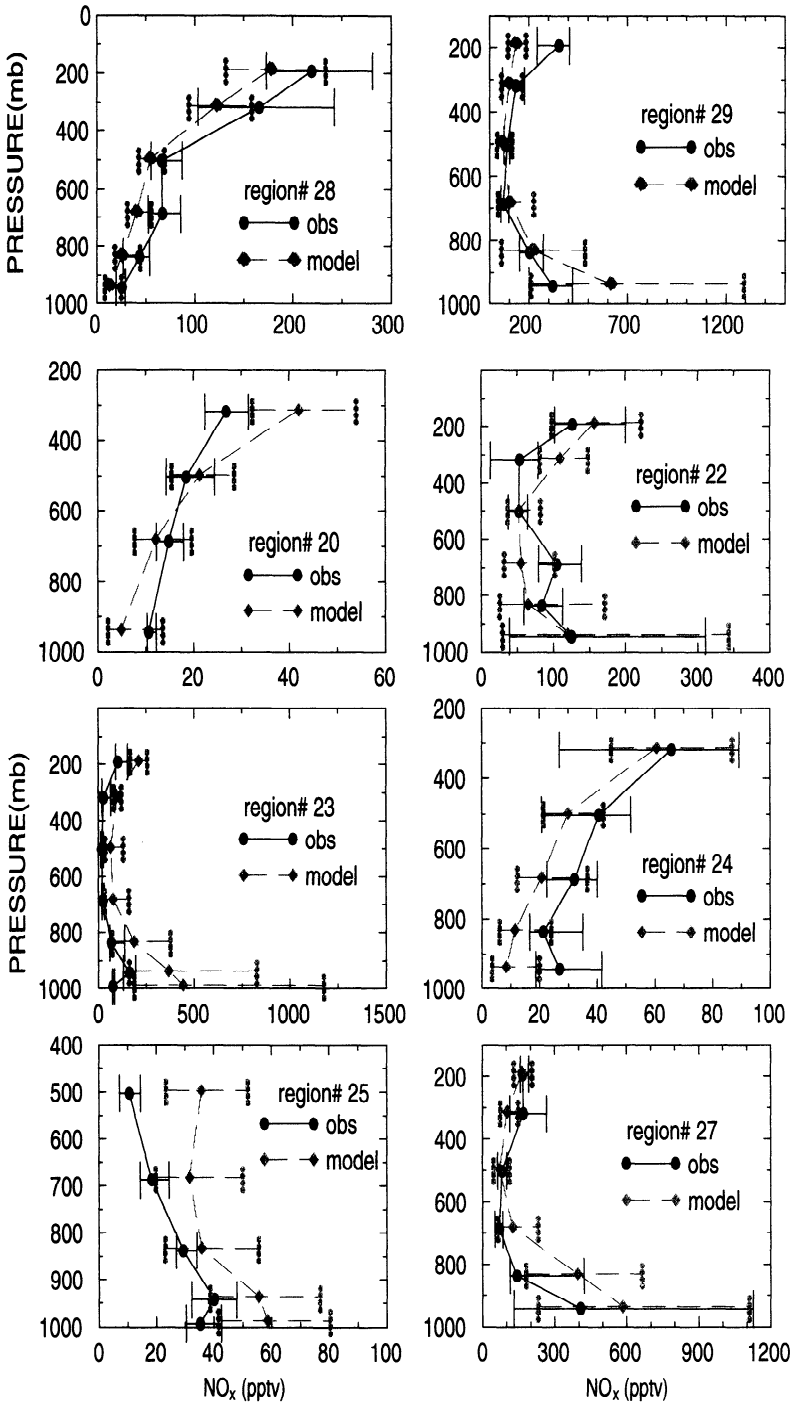

Figure 7. (continued)

er hand, the simulated and measured sums (NO_x + HNO_3 + PAN) are in reasonable agreement, as are simulated and measured HNO_3. Simulated NO_x, while only moderately lower than measurements during winter and spring, is much lower in summer and fall, with almost no overlap between the simulated and observed IQRs. However, simulated PAN is systematically higher than observed, and the simulated and the measured sums ($NO_{x\ median}$ + PAN_{median}) are in good agreement. Since this pair should be in thermal balance at moderate temperatures (e.g., PAN has a 12 hour thermal decomposition lifetime at 8°C), it is possible that the GCTM's systematically lower NO_x and higher PAN are due to the GCTM's 685 mbar summertime temperatures in the FT (~3°C) being significantly lower than those at MLO (7°-8°C). The extremely low PAN levels observed during the summer suggest either contamination by maritime BL air or local heating. Heterogeneous conversion of HNO_3 to NO_x has also been suggested by *Hauglustaine et al.* [1996b], but with no systematically low NO_x bias for the rest of the world (see section 3.2.2), the postulated heterogeneous conversion would have to be local to MLO. While an additional heterogeneous loss of HNO_3 on dust may be supported by some recent observations

Table 2. Surface NO_x Medians and Interquartile Ranges (IQR)

Station	Latitude, deg	Longitude, deg	Season	GCTM Median, IQR ppbv	GCTM Range, ppbv	Observed Median, IQR ppbv	Observed Range, ppbv	Reference
Scotia, PA	41N	78W	July-Aug.	1.84	2.74-1.28	1.38	3.12-0.87	1
Bondville, IL	40N	88W	Aug.	2.37	3.24-1.70	1.53	2.79-0.97	1
Candor, NC	35N	80W	Aug.	1.48	2.07-0.97	0.86	1.09-0.72	1
Egbert, Ont.	44N	80W	July-Aug.	1.81	2.58-1.03	0.92	3.26-0.45	1
Harvard Forest	42N	72W	Dec.-Feb.	1.82	3.03-0.77	3.48	10.59-1.61	1
			March-May	1.00	2.00-0.54	1.63	4.31-0.70	1
			June-Aug.	1.30	1.83-0.67	0.67	1.24-0.50	1
			Sept.-Nov.	1.35	2.11-0.62	2.08	5.54-0.82	1
Sable Island	44N	60W	Aug.-Sept.	0.079	0.129-0.012	0.079	0.138-0.044	1
1992 ASTEX, eastern N. Atlantic			June (range/mean)	0.004 - 0.010		0.032 ± 0.020		2
SAGA 3 Cruise, Equatorial Pacific			Feb.-March (range)	0.003 - 0.012		0.005 - 0.010		3

1, *Emmons et al.* [1997]; 2, *Carsey et al.* [1997]; 3, *Torres and Thompson* [1993]. ASTEX, Atlantic Stratocumulus Transition Experiment; SAGA, Soviet-American Gas and Aerosol Experiment.

[*Tabazadeh et al.*, 1998], recent modeling studies do not support the heterogeneous conversion of HNO_3 to NO_x [*Singh et al.*, 1998; *Wang et al.*, 1998a,b].

4. Simulated Tropospheric NO_x

Having examined the GCTM simulations of NO_x to the extent that available measurements allow and finding that they appear to be realistic, we will now explore their global behavior and quantify the contributions from individual sources. All simulations have been run for 18 months, and the last 12 months are used for analysis. Both the annual NO_x sources and sinks are in balance to within 1% or better, and the monthly mean NO_x fields are changing by less than 1% from one year to the next. In order to minimize any nonlinear effects, the NO_x fields for an individual source are determined by subtracting the NO_x fields generated by a simulation excluding that particular source from fields simulated with all six sources.

4.1. Global NO_x Distributions

The key features of our simulated NO_x fields can be seen in Figure 8, where June - August (JJA) and December - February (DJF) seasonal means are presented for the surface (990 mbar), lower (685 mbar), middle (500 mbar), and upper (315 mbar) troposphere.

The maxima in the surface NO_x fields are quite similar to those in the source (see Figure 2b) and are repeated throughout the BL (990, 940, 835 mbar). The main spatial features are the high levels over the midlatitude continents (>0.5 ppbv) and very low levels (0.01 ppbv) over the southern oceans. The primary seasonal features are the seasonal tropical maxima (> 0.5 ppbv) that follow the tropical biomass burning season and the extensive spread of moderate levels of NO_x (0.05 ppbv) over the oceans north of 30°N during the NH winter. This spread is a result of both increased wintertime transport in the midlatitude troposphere and increased NO_x chemical lifetime (see Figure A3 in the appendix). The seasonal and spatial patterns in the lower troposphere (685 mbar) are similar to those in the BL, although the gradients are weaker.

Moving up to 500 mbar, we find fields that are more zonally uniform for both DJF and JJA, with NO_x less than 20 pptv south of 30°S and 20 - 50 pptv to the north of 30°S. The exceptions are regional maxima associated with areas of intense local convection and areas of strong lifting along wintertime storm tracks. With lightning absent in the wintertime midlatitudes, those maxima would appear to result from transported BL NO_x, while the tropical and the summertime midlatitude maxima would appear to be a mixture of convective pumping

Table 3. MLOPEX Observed and Simulated Medians and Interquartile Ranges (IQR)

	Winter 1992 Median	Winter 1992 IQR	Spring 1992 Median	Spring 1992 IQR	Summer 1992 Median	Summer 1992 IQR	Fall 1992 Median	Fall 1992 IQR
NO_y, pptv								
GCTM	147	288-74	170	254-106	129	197-95	105	146-63
Observed [NO_y]	187	258-138	374	431-305	188	258-132	168	207-131
Observed [NO_x+PAN+HNO_3]	119		196		98		106	
HNO_3, pptv								
GCTM	87	122-41	87	128-52	95	153-69	66	91-40
Observed	64	100-30	132	203-71	67	102-44	75	95-49
NO_x, pptv								
GCTM	24	42-15	22	34-13	12	18-9	13	21-8
Observed	30	40-23	35	52-28	27	39-19	23	32-20
PAN, pptv								
GCTM	39	118-14	60	103-29	21	30-15	20	40-11
Observed	25	39-10	28	57-10	4	11-1	8	17-4
$NO_{x\,median}$ + PAN_{median}, pptv								
GCTM	63		82		33		33	
Observed	55		63		31		31	

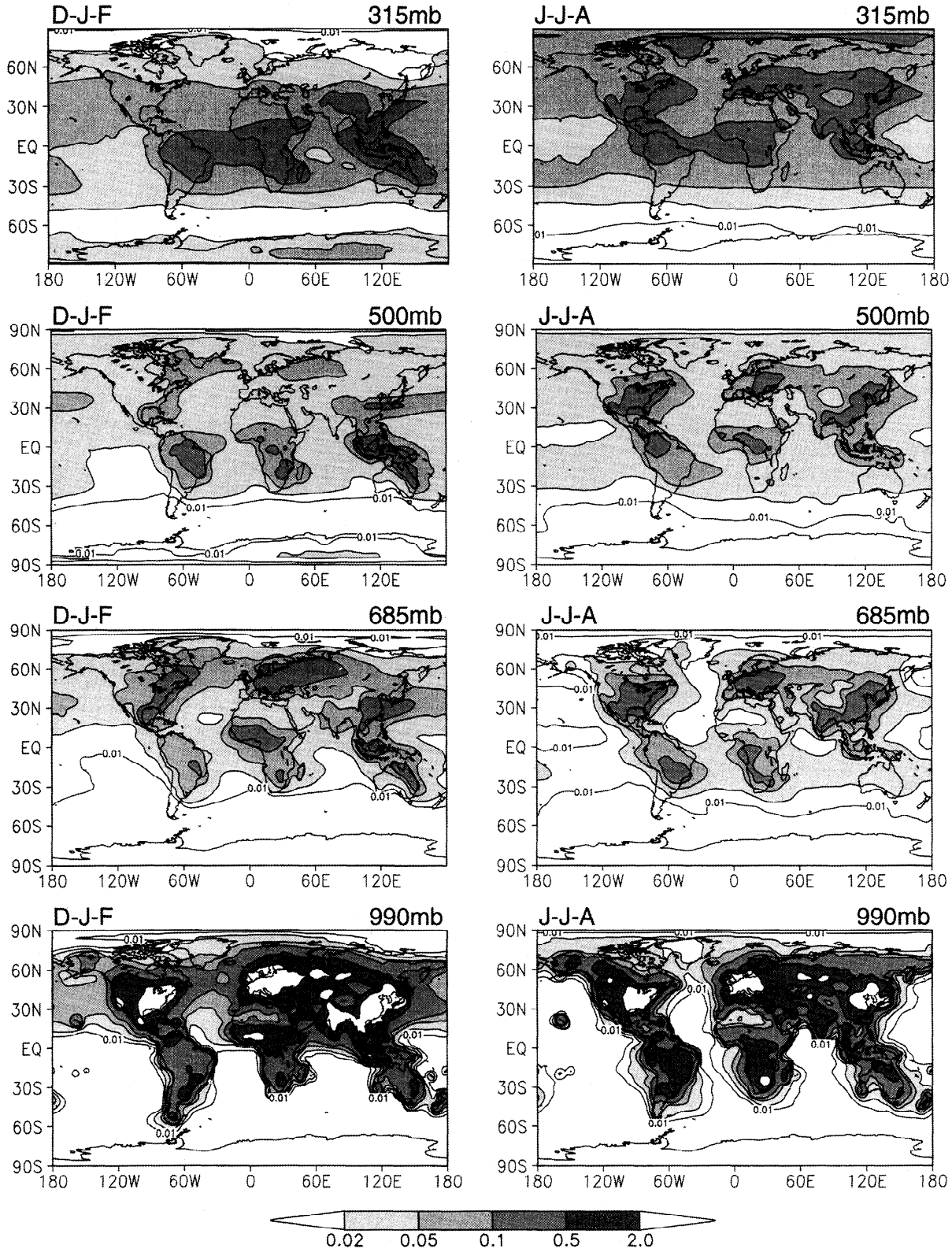

Figure 8. December through February (D-J-F) and June through August (J-J-A) simulated seasonal-average NO_x mixing ratios (ppbv) presented for the GCTM upper troposphere (315 mbar), midtroposphere (500 mbar), lower troposphere (685 mbar), and surface level (990 mbar).

of BL NO_x and 500 mbar lightning. These source apportionment questions will be examined in detail in the next section.

The upper troposphere (315 mbar) has seasonal patterns similar to 500 mbar with generally higher values. For both seasons there is a basic zonal distribution of NO_x upon which two major features are superimposed: (1) There are maxima in the tropics and summertime continental midlatitudes, which are regions strongly influenced by deep convection and where an earlier paper [*Levy et al.*, 1996, Figures 5 and 6] found lightning emissions of NO_x to play a major role, (2) There are wintertime minima and summertime maxima at high latitudes, which run counter to the model's seasonality of cross-tropopause transport of NO_y [*Mahlman and Moxim*, 1978; *Levy et al.*, 1979]. This second feature results from the much higher fraction of NO_y found as NO_x in the summertime lower stratosphere and upper troposphere, due primarily, to the much stronger photodissociation of HNO_3 in summer. The 190 mbar levels (not shown in Figure 8) have the same seasonal NO_x patterns as 315 mbar with higher overall levels, but only the tropical region (30°N-30°S) normally remains in the troposphere.

4.2. Boundary Layer Versus Free Troposphere

We now focus on a key issue in GCTM simulations of NO_x: the relative contributions of the large BL sources and the much smaller FT sources to NO_x levels throughout the troposphere. The surface sources control the levels in the polluted BL. In the remote maritime BL, both BL and FT sources contribute, with transport by PAN playing a major role [*Moxim et al.*, 1996], but NO_x levels are generally so low (see Figure 8) that ozone destruction dominates and none of the sources has a significant impact on tropospheric chemistry. However, the relative impact of BL and FT sources on the moderate levels of NO_x in the FT, where net ozone production or destruction is in the balance, is a complex issue. A key factor is subgrid-scale vertical transport from the continental BL source regions by convection. We parameterize this by a stability-dependent diffusion and find that the resulting vertical profiles of Rn and CO in the GCTM are quite realistic. See the appendix and Figures A1 and A2 for a detailed discussion.

In Figure 9 we examine the extent to which the three BL sources, which exceed the in situ FT sources by almost a factor of 8, influence NO_x levels in the FT during DJF and JJA. Starting in the lower FT (685 mbar), we see that in DJF, the BL NO_x sources completely dominate in the NH, while during JJA, they dominate over broad extratropical belts in both hemispheres. FT sources dominate in much of the tropics throughout the year, while the broad white areas in the southern hemisphere (SH) and over the remote oceans represent regions with $NO_x < 10$ pptv.

At 500 mbar, BL sources still provide more than 40% of the NO_x throughout the NH extratropics and more than 60% of the NO_x in NH high latitudes during DJF. There is also a small westerly plume of more than 40% BL NO_x at 500 mbar over the extratropical South Atlantic during DJF. In JJA there is a much larger tropical and extratropical westerly plume of BL NO_x off South America and Africa showing up during the SH burning season at both 315 and 500 mbar. In most of the tropics (30°N-30°S), FT sources strongly dominate all year, with the exception of intensely convective areas over land, where BL sources are still providing more than 40% of the NO_x. The broad white areas in the SH extratropics represent regions with $NO_x < 10$ pptv.

In the upper troposphere, FT sources increase their control over most of the 315 mbar level, though BL sources continue to provide more than 60% of the relatively low NO_x levels in the wintertime high latitudes. In the NH, this results from poleward transport of NO_x by winter and spring storms from midlatitude source regions into a region with long NO_x lifetimes (see *Moxim et al.* [1996, section 3.4] for a detailed discussion). There is still a broad white belt of $NO_x < 10$ pptv near the SH pole during JJA. At 190 mbar, BL sources play almost no role, with the exception of the intensely convective regions over the tropical continents where a small westerly plume extends over the Indian Ocean during DJF and over the western Pacific during JJA.

4.3. Individual Source Contributions

While we discussed the global impact of 3 TgN/yr of lightning emission on troposphere NO_x in an earlier paper [*Levy et al.*, 1996, Figures 5 and 6], this is our first complete and unified discussion of individual source contributions to tropospheric NO_x. In Plate 1, we examine color-coded maps displaying the source which supplies the most NO_x to a particular grid box. While a displayed source need only supply a plurality of NO_x to be displayed, it generally is the majority supplier of NO_x away from a color border. Near the borders the two or three neighboring colors supply comparable levels of NO_x. The white areas represent regions with $NO_x < 10$ pptv, where it plays no significant role in tropospheric chemistry [see *Klonecki and Levy*, 1997]. We only include DJF and JJA, since these two seasons capture the important features of regional source dominance.

At the surface, fossil fuel combustion supplies the majority of the NO_x over most of the NH throughout the year. In the tropics, biomass burning supplies the majority during the dry seasons, and soil-biogenic emission supplies the majority during the wet seasons. In JJA, either biomass burning or soil-biogenic emissions are dominant over remote continental regions in the NH extratropics. Note the dominant role for soil-biogenic emission (green) over the agricultural regions of the great plains in western United States and Canada and in central Russia and the biomass burning dominance (red) over the northern forests of Alaska, Canada, and Russia.

Moving up to the lower FT, we find that fossil fuel combustion still supplies the majority of the NO_x over much of the NH at 685 mbar during both seasons, and biomass burning dominates in the tropics during their burning seasons with a large plume over the Southern Ocean during summer. Biogenic emissions, while still important in the tropics during their wet seasons and over extratropical agricultural lands in the summer, are no longer the largest contributor except for a few locations. Lightning now supplies the majority of NO_x at 685 mbar in much of the tropics.

In the midtroposphere (500 mbar) the role of individual NO_x sources simplifies, with fossil fuel combustion suppling the majority of NO_x in the NH extratropics throughout the year and lightning doing the same in the tropics and SH subtropics. There is still a plume of dominance by biomass burning over the Southern Ocean in JJA.

It becomes more complicated in the upper troposphere (315 mbar), where five of the six sources control different regions in different seasons. The dominant sources during DJF are BL fossil fuel combustion and in situ emissions from aircraft in the NH extratropics, lightning emissions from 30°N to ~45°S, and stratospheric injection in the SH high latitudes. In JJA,

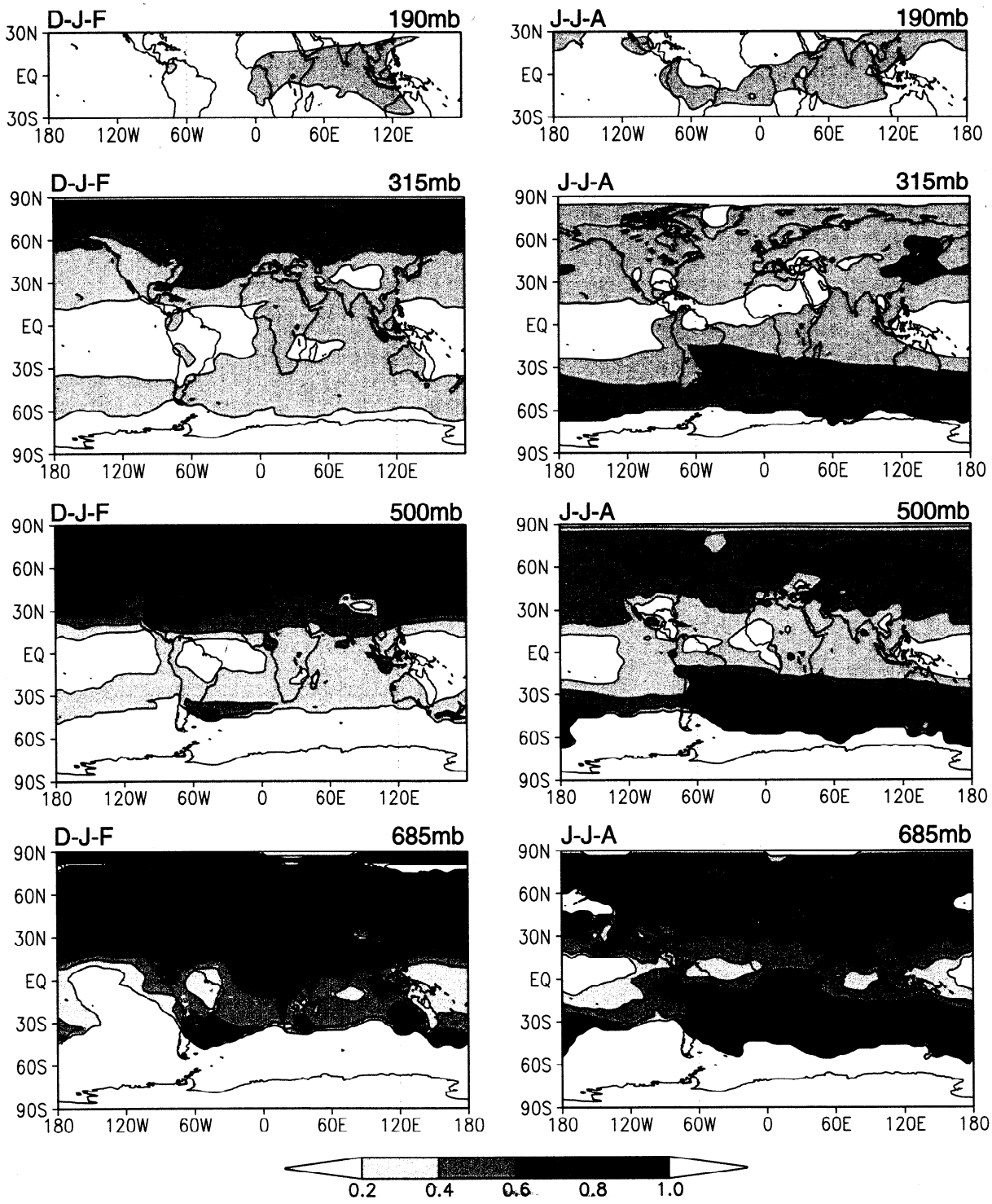

Figure 9. Simulated December through February (D-J-F) and June through August (J-J-A) fractional contributions of the BL sources (fossil fuel combustion, biomass burning, soil biogenic emission) to the NO_x levels in the free troposphere (685, 500, 315, and 190 mbar between 30°N and 30°S). Note that the white area in the SH at 685 and 500 mbar and during summer at 315 mbar represents regions where NO_x is less than 10 pptv and plays no significant role in atmospheric chemistry.

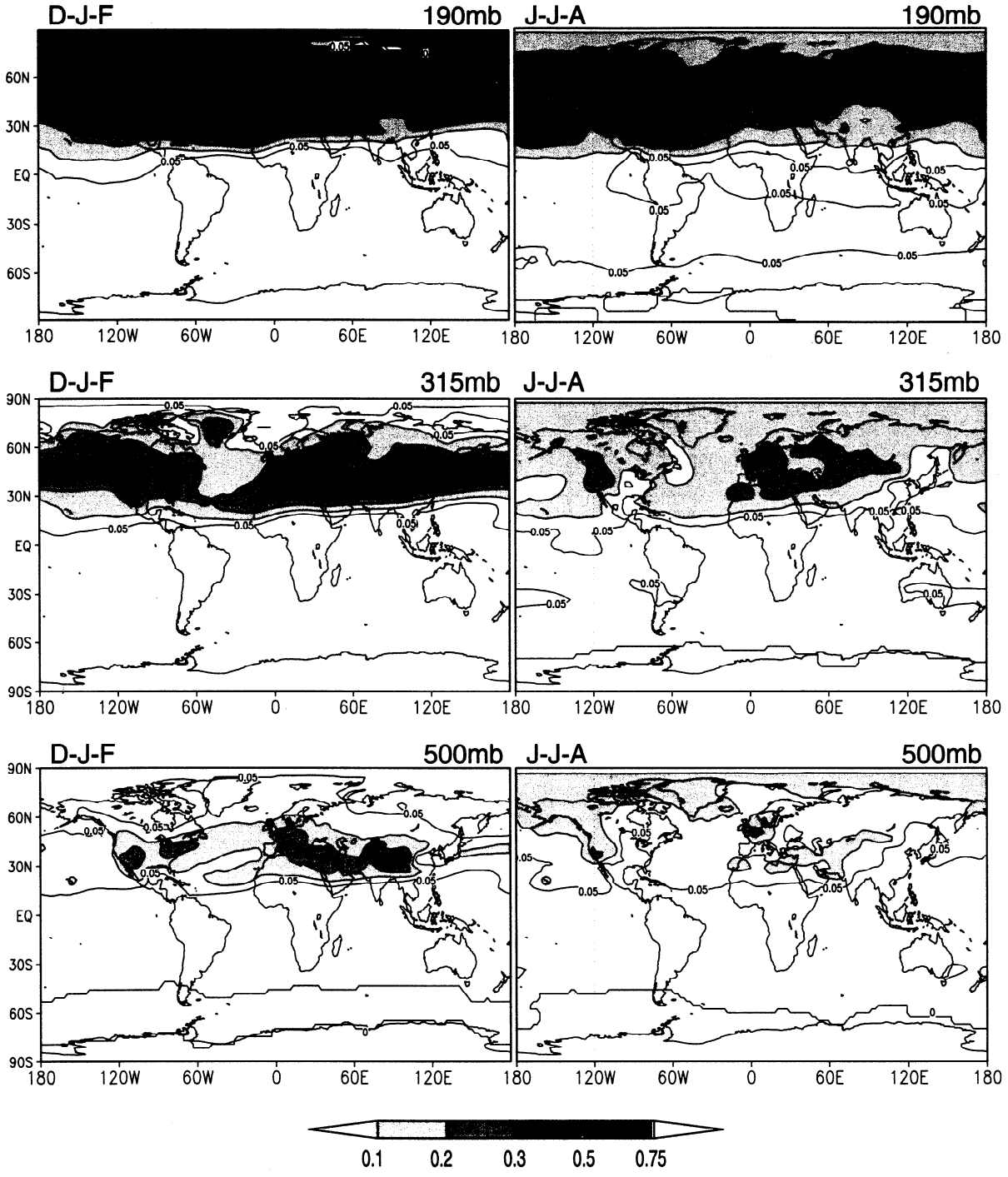

Figure 10. Fractional contributions of the aircraft emission source to simulated NO_x levels in the 190, 315, and 500 mbar levels during December through February (D-J-F) and June through August (J-J-A).

stratospheric injection dominates the NH high latitudes, and lightning dominates in a broad belt from ~45°N to ~40°S, while stratospheric injection, biomass burning, and BL fossil fuel combustion all play a role in the SH high latitudes. In the tropical upper troposphere (190 mbar, which is not shown in Plate 1), lightning dominates throughout the year. Note that stratospheric injection, while generally strongest in the winter of each hemisphere, only supplies a majority of the NO_x in the summer, when NO_x is a significant fraction of the incoming stratospheric NO_y. This point was discussed previously in section 4.1.

4.4. Aircraft Emissions

The impact of aircraft emissions on tropospheric NO_x, which has been the subject of considerable research interest in the last few years [e.g., *Thompson et al.*, 1996; *Friedl*, 1997], is presented in Figure 10 for DJF and JJA. These in situ NO_x emissions make their largest contribution in the NH extratropical lower stratosphere (190 mbar), where they contribute over 50% of the wintertime NO_x and 20 - 50% in the summer, with the largest summertime impact over the North Atlantic and Europe. Dropping down to the NH extratropical upper tropo-

Table 4. Source Contributions to NO_x Levels in the TRACE-A Area

Region	Fossil Fuel	Biomass	Biogenic	Lightning	Aircraft	Stratosphere
E. South America						
FT	6	31	12	46	1	4
BL	12	65	20	3	<1	<1
S. Atlantic						
FT	5	20	11	59	2	3
BL	5	69	17	8	<1	1
South Africa						
FT	5	31	11	46	2	5
BL	10	70	17	3	<1	<1

Values are in units of percent. FT, free troposphere; BL, boundary layer.

sphere (315 mbar), in situ aircraft emissions contribute 20-50% of the wintertime NO_x in a NH midlatitude belt and ~20% of the NO_x over Europe in the summer. Aircraft supply no more than 5-10% of the summertime NO_x in the NH at 500 mbar and have almost no impact (< 5%) throughout the SH and below 500 mbar in the NH.

4.5. Regional Studies of Individual Source Contributions

The previous sections provided a global picture of source contributions to our simulated NO_x fields. We now examine two areas that have been the subject of major observational campaigns and compare their analysis of individual source contributions with our GCTM results.

The first area is based on the TRACE-A campaign, which occurred during September and October of 1992. The area is composed of regions 27 (South Africa), 28 (South Atlantic Ocean), and 29 (eastern South America), which are described in Figure 4 and Table 1. In this area we sample both the direct impact of tropical BL sources as well as a more remote ocean region with few local sources. The South Atlantic FT (region 28) is of special interest due to its well-known ozone maximum which occurs during the area's biomass burning season [*Fishman et al.*, 1990]. We first examine the NO_x distributions in the TRACE-A area via the summer panels of Figure 8, which have similar patterns to those simulated for September and October though the maxima are smaller. In the BL, NO_x is concentrated over land, with very low mixing ratios over the South Atlantic. As we move up in the troposphere, NO_x begins to spread over the South Atlantic in subtropical westerly flow from the source regions of South America and in tropical easterly flow from the source regions of southern Africa. By 315 mbar, a band exceeding 100 pptv has spread across the tropical South Atlantic. The percentage contributions of each source to the volume integral of NO_x for both the FT and BL are given in Table 4. Throughout the FT, lightning plays the dominant role, contributing ~50%, while biomass burning and soil biogenic emissions, both of which have been lifted from the BL, contribute 20-30% and 10%, respectively. Biomass burning dominates in the BL with 65-70%, while biogenic emissions and fossil fuel combustion supply ~20% and ~10%, respectively. Our source apportionment, particularly in the FT over the South Atlantic region, is consistent with the analyses of TRACE-A observations by *Smyth et al.* [1996], *Singh et al.* [1996a], *Talbot et al.* [1996], and *Pickering et al.* [1996].

The second area to be examined is based on the PEM-West A and B campaigns, which occurred in September-October of 1991 and February-March of 1994, respectively. Our selected area includes regions 17, 23 (Japan); 16, 22 (oceanic SE Asia); and 18, 24 (tropical North Pacific), which are described in Figure 3 and Table 1. While this area, with the exception of Japan, has few local sources, it is just downwind of and strongly influenced by the Asian BL sources. It has been argued that, relative to PEM-West A, PEM-West B experienced enhanced outflow from the polluted Asian BL [e.g., *Hoell et al.*, 1997], and their meteorological analysis as well as both their observed and our simulated sums of NO_x, HNO_3, and PAN (see Figure 5) support this view. However, throughout most of the area, neither simulated nor measured NO_x shows any significant increases during PEM-West B. In fact, the PEM-West A NO_x values are frequently larger. This would suggest that, while there may be enhanced Asian outflow during PEM-West B, it does not lead to enhanced NO_x levels and the resulting enhancement of chemical reactivity.

In Table 5 we see that, during both measurement periods, fossil fuel NO_x totally dominates the BL in the Japan region and also dominates in oceanic SE Asia, though biomass burning does supply ~20% during PEM-West B. The BL NO_x mixing ratios of the tropical North Pacific region are quite small (see Figure 8), with lightning and fossil fuel as the dominant sources during both PEM-West campaign periods, though biomass burning again supplies~20% during PEM-West B. In the FT, simulated NO_x levels in the Japan region are controlled throughout both campaigns by the fossil fuel source, both in situ and transported from Asia, while lightning dominates FT NO_x in the other two regions. This dominant role for lightning is consistent with the conclusions and inferences of *Singh et al.* [1996b] in PEM-West A and *Kawakami et al.* [1997] in their analyses of the PEM-West B data.

Unlike the TRACE-A regions, eastern and southeastern Asia are subject to transient synoptic-scale weather disturbances during winter and spring, similar to the U.S. East Coast. These storms transport air northeastward and upward ahead of them, and their attendant cold fronts advect surface air offshore south and east behind them [see *Moxim et al.*, 1996, section 3.4]. These transport effects can be inferred from Table 5, when we examine the influence of winter biomass burning from southeast Asia on all three PEM-West B regions. Biomass NO_x affects the Japan region almost exclusively in the FT, both in percentage and actual mixing ratio, which implies lifting during its northeastward transport. Farther south in oceanic SE Asia, the largest biomass impact occurs in the BL, indicating direct BL transport from the continent. Remnants of these winter-spring transport events even reach the tropical North Pacific BL.

Table 5. Source Contributions to NO_x Levels in the PEM-West A and B Areas

Regions	Fossil Fuel		Biomass		Biogenic		Lightning		Aircraft		Stratosphere	
	A	B	A	B	A	B	A	B	A	B	A	B
Japan region												
FT	62	56	5	12	4	3	16	10	8	9	5	10
BL	96	96	2	2	1	1	1	-	-	1	-	-
Oceanic SE Asia												
FT	20	12	2	8	5	4	66	70	4	4	3	2
BL	79	65	2	17	9	8	9	10	1	-	-	-
Tropical N. Pacific												
FT	10	8	3	8	4	5	75	73	5	4	3	3
BL	32	43	3	19	9	6	54	30	1	1	1	1

A and B represent PEM-West A and PEM-West B, respectively. Values are in units of percent.

5. Analysis of Uncertainty

The major sources of uncertainties in both the simulated NO_x fields and their resulting source apportionment are errors in the GCTM simulated transport that controls the long-range export of NO_x, errors in the magnitude and timing of NO_x emissions, incomplete and/or inaccurate simulation of dry and wet deposition, errors or incompleteness in the chemical processes that control NO_x chemical production and destruction.

The key grid-scale and subgrid-scale transport issues are discussed in the appendix and section 3. While no GCTM model, including our own, is without regional flaws, there appear to be no major problems. The next two possible sources of error, BL NO_x emissions and depositions, are highly correlated in the BL source regions, with the difference between emission and local deposition representing the reactive nitrogen available for export to the remote troposphere. The sources are discussed in the appendix and in detail in previous papers. As discussed in section 3, NO_x levels in BL source regions and in the FT are not sensitive to uncertainties in precipitation removal, and there are no biases downwind of the BL sources. This leaves FT production of NO_x by lightning, whose global magnitude is still a matter of some debate [*Levy et al.*, 1996 and references therein; *Price et al.*, 1997]. Our analysis found that the global source strength was relatively tightly bounded. This bound was not sensitive to uncertainties in either BL sources or wet and dry removal, but was dependent on simulated OH levels in the lightning production regions.

The major sources of uncertainty rest with the chemistry simulation. The inclusion of a realistic PAN simulation ensures the major source of NO_x in the remote lower troposphere [*Moxim et al.*, 1996]. This leaves our simulation of OH, which controls NO_x chemical lifetime, strongly affects local NO_x levels, and may affect its export around the globe, as the key area of concern. The three major OH issues are zonal OH fields; no non-H_2O HO_x sources and low FT humidities; and a CH_3CCl_3 lifetime of 6.3 years, rather than the recently revised 4.8 years.

Since NO_x, O_3, and surface albedos are all generally elevated over land and depressed over the ocean, our zonal-average OH fields understate NO_x destruction over the continental source regions and overstate it over the remote oceans. As a result, our simulated BL NO_x levels are too high over source regions, which Table 2 confirms. The impact of nonzonal OH on NO_x levels over the ocean is not clear. While the amount available for transport from BL sources would be reduced, so is NO_x destruction over the ocean. With no particular bias between observations and the simulation downwind of BL sources or in the FT, it would appear that the nonzonal OH features tend to cancel when it comes to the export of BL NO_x. Possibly more serious issues lie in the details of the OH chemistry itself.

In the upper troposphere, our OH chemistry does not include the contribution of acetone oxidation to upper tropospheric HO_x [*Singh et al.*, 1995], the upper troposphere water vapor concentrations in the OH calculation are significantly dryer than those inferred from satellite observations (B. Sodcn, private communication, 1997), and recent upper tropospheric observations find that OH levels should be 50 - 100% higher than those calculated with a chemical model similar to the one used for this GCTM upper troposphere [e.g., *Jaegle et al.*, 1997]. In a recent preliminary simulation incorporating these corrections, OH levels in the upper troposphere increased by as much as a factor of 2-3, with an average of ~50% [*Klonecki*, 1998]. While this would require our increasing the global lightning source to 8-10 TgN/yr, it would not significantly alter the upper tropospheric distribution of NO_x and would only strengthen the major role of FT sources, lightning in particular, in the free troposphere.

The recent reduction in the estimated CH_3CCl_3 lifetime from ~6.2 years [*Prinn et al.*, 1987], with which our OH fields agreed, to ~4.8 years [*Prinn et al.*, 1995] implies an ~30% increase in the globally averaged tropospheric OH. Recent GCTM sensitivity studies found this produced a 10-17% decrease in simulated NO_x levels around the globe [*Klonecki*, 1998, chap. 5.2.2]. This level of uncertainty in overall OH levels will not significantly affect the global NO_x fields, and the decreased NO_x chemical lifetime would only further decrease the impact of BL sources on the FT.

6. Conclusions

The GCTM's HNO_3 wet deposition, with the exception of outliers due to either anomalous local observations or local errors in the GCTM's NO_x source and simulated precipitation, is highly correlated to the observations and clearly captures the observed spatial patterns of wet deposition. However, there appears to be a significant positive bias (~20%) in the simulated U.S. deposition, though not for the rest of the world. The GCTM's NO_x fields are in reasonable agreement with the large majority of the available observations (~50% of the comparisons within ±25% of the 1:1 line and ~75% within ±50%), show no systematic global biases, display the observed vertical profiles, have high levels (~1 ppbv or greater) in the polluted BL, and have very low values in the remote

BL. At Mauna Loa Observatory, while summer and fall simulated NO_x is clearly in deficit, the PAN is in surplus, and the sum of the two agrees well with observations. In general, the level of agreement between simulation and observation is as good as the agreement between separate, but simultaneous, observations of NO, NO_x, or NO_y. We conclude that the simulation of global tropospheric NO_x is generally realistic.

The BL sources of NO_x, which are primarily anthropogenic, exceed FT emissions, which are primarily natural, by more than 8:1 and completely dominate BL tropospheric NO_x levels, excepting very remote regions, where BL and FT sources have a comparable impact. In the FT, the smaller FT sources play a larger role and generally dominate in the upper troposphere. Considering individual sources, anthropogenic emissions from surface fossil fuel combustion and biomass burning dominate in the BL, with a significant contribution from biogenic emissions in remote regions that do not have biomass burning. In the lower troposphere, surface fossil fuel combustion dominates in the NH extratropics, lightning is the primary source in the tropics, and biomass burning plays a major role in much of the SH. In the middle troposphere, lightning dominates in the tropics and the summertime midlatitudes, while transported surface fossil fuel combustion supplies the NH high latitudes, and transported emissions from biomass burning do the same in much of the SH. In the upper troposphere, lightning's dominance spreads even farther poleward, while surface fossil fuel combustion and stratospheric injection are the major sources in the respective winter and summer NH high latitudes. Remnants of biomass burning, along with stratospheric injection, dominate in the SH high latitudes. Although seldom dominant, aircraft emissions do play a significant role in the upper troposphere and lower stratosphere of the NH extratropics.

Our simulated NO_x distribution's agreement with available observations and individual source contributions appear to be insensitive to uncertainties and errors in transport, sources, deposition, and chemistry. Our conclusions regarding the dominant role of relatively small in situ FT sources, primarily lightning, throughout much of the FT was also robust. Lowered estimates of the CH_3CCl_3 lifetime and the nonwater sources of HO_x in the upper troposphere would increase the simulated level of OH and increase the global scaling of the lightning source of NO_x. Both would only decrease the transport of NO_x from the BL and enhance the role of lightning.

Appendix: Detailed Description of NO_x GCTM

Our GCTM was developed at the Geophysical Fluid Dynamics Laboratory (GFDL) [*Mahlman and Moxim*, 1978; *Levy et al.*, 1982, 1985; *Levy and Moxim*, 1989a,b]. In a joint effort between GFDL and the Georgia Institute of Technology to simulate the tropospheric chemistry of reactive nitrogen, it has been used to study the individual NO_x sources [*Kasibhatla et al.*, 1991; *Levy et al.*, 1991; *Kasibhatla*, 1993; *Kasibhatla et al.*, 1993; *Levy et al.*, 1996], the behavior of reactive nitrogen compounds in the northern high latitudes [*Levy et al.*, 1993], the present and future global deposition of oxidized nitrogen [*Galloway et al.*, 1994], the impact of NO_x emissions on the present and future global biogeochemical cycle of nitrogen [*Galloway et al.*, 1995], the impact of PAN transport and chemistry on NO_x levels away from continental sources [*Moxim et al.*, 1996], and the impact of anthropogenic NO_x emissions on the summertime levels of tropospheric ozone over the North Atlantic [*Kasibhatla et al.*, 1996] and global tropospheric ozone budgets [*Levy et al.*, 1997].

A1. Grid-Scale Transport

The large-scale transport is driven by the parent GCM's resolved winds [*Manabe et al.*, 1974; *Manabe and Holloway*, 1975], which are given in sigma (terrain following) coordinates, and is integrated in flux form, using a centered leapfrog numerical scheme which is second order in the horizontal and fourth order in the vertical. The global integrals of both the tracer mixing ratio (R) and its square (R^2) are conserved during advection. A detailed discussion of the scheme is given by *Mahlman and Moxim* [1978, section 3]. The GCTM cannot realistically simulate atmospheric fluctuations with periods shorter than 6 hours, nor can it generate diurnal or interannual variability. However, most large-scale resolved processes, such as interhemispheric exchange, monsoonal flows, and north-south transport by midlatitude storms, are both present and well represented without any explicit tuning [e.g., *Moxim et al.*, 1996, appendix section 3.4]. However, having only 1 year of simulated weather results in a number of regional differences between the GCTM's transport and that which is observed for a particular year. While these differences have an impact on the GCTM's simulation of summertime transport over the U.S. Gulf Coast and the near western North Atlantic Ocean, they do not significantly affect transport to the remote troposphere.

A number of relatively simple chemical tracers have been employed to evaluate the GCTM's large-scale tropospheric transport (S.-M. Fan, private communication, 1997). Seasonal cycles of CO_2, which were simulated with terrestrial net primary productivity based on the Carnegie, Ames, and Stanford Approach (CASA) biospheric model [*Potter et al.*, 1993], compared well with observed seasonal cycles at Barrow, Alaska; Shemya, Alaska; Azores; Niwot Ridge, Colorado; Mauna Loa, Hawaii; and Ascension Island [*GLOBALVIEW-CO_2*, 1996]. The GCTM's simulation of Kr^{85} in the surface layer over the Atlantic, which employed 1978-1981 emission rates from *Jacob et al.* [1987], agreed quite well with observations from the R/V *Meteor* 1980/1981 Atlantic Ocean cruise between 35°S and 48°N [*Weiss et al.*, 1983]. The GCTM's simulation of SF_6 (see *Denning et al.* [1999] for details of the source and observations) realistically reproduced the observed interhemispheric gradient, growth rates, and transport-induced levels of variability in SF_6 time series from remote locations (S.-M. Fan, private communication, 1997; *Denning et al.* [1999]). In all these studies, we find that the GCTM, without benefit of any explicit tuning of subgrid-scale parameterizations, realistically reproduces the observed interhemispheric gradients for all the tracers, the transport-dominated seasonal behavior of CO_2 and SF_6 at remote sites and the growth rates and transport-induced levels of variability in SF_6 time series from remote locations.

A2. Subgrid-Scale Transport

A universal difficulty for all simulations of global atmospheric transport is the numerical treatment of a wide range of subgrid-scale atmospheric processes. While our medium resolution GCTM is able to simulate the large-scale synoptic features of weather, it is not able to resolve the finer details, nor does it realistically represent squall lines or capture moist

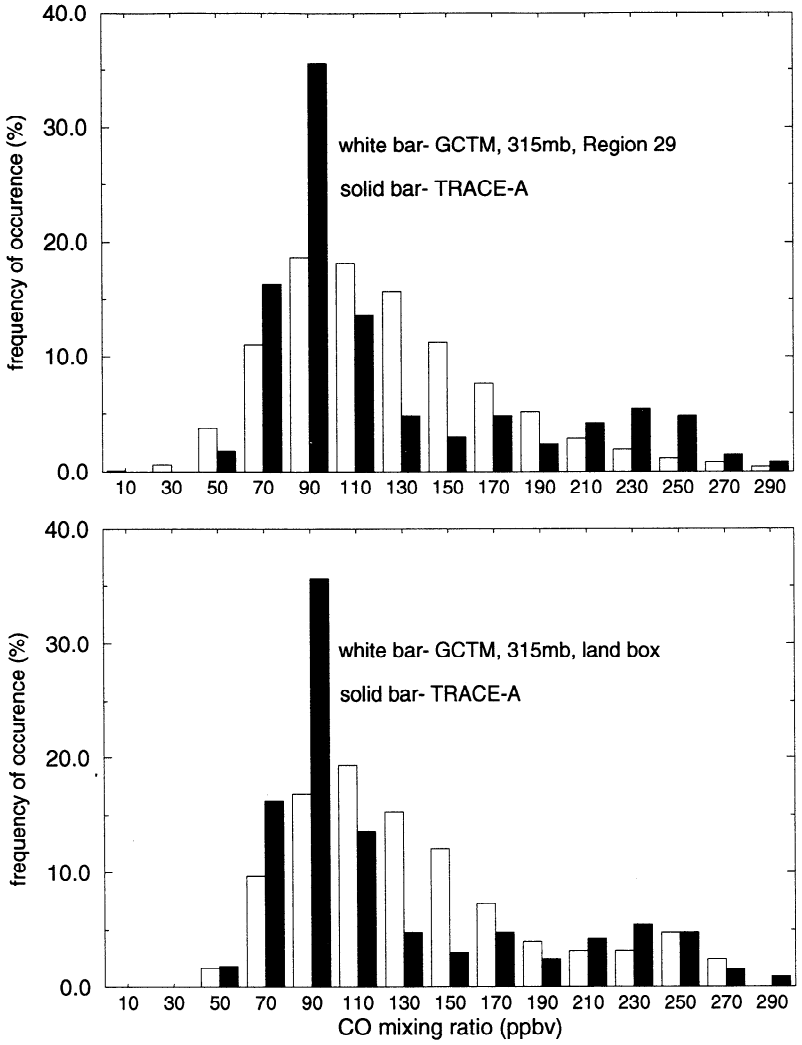

Figure A1. Simulated frequency distributions of CO mixing ratios for a convectively influenced region. (a) Frequency distributions of 331 upper tropospheric (7.5-11.5 km) measurements from TRACE-A over and off the coast of Brazil (flights 5-7) and from the GCTM level 315 mbar at the same time and location. (b) Frequency distributions of 331 upper tropospheric (7.5-11.5 km) measurements from TRACE-A over and off the coast of Brazil (flights 5-7) and from a GCTM 315 mbar grid box over Brazil.

convection and turbulence on their observed scales. These processes are subgrid-scale and must be represented by parameterizations that are based on resolved grid-scale variables. In all cases, including this study, the parameterizations are approximate physical representations of the actual processes.

Particularly challenging has been the grid-scale representation of vertical transport by convective clouds, which are very important in the tropics and the summertime continental midlatitudes. While a number of nondiffusive parameterizations have been developed [e.g., *Chatfield and Crutzen*, 1984; *Tiedtke*, 1989; *Jacob and Prather*, 1990; *Allen et al.*, 1997] which instantaneously transport significant fractions of BL air into the upper troposphere, we prefer to employ a stability-dependent diffusive parameterization that attempts to capture the ensemble average of convective events in a given grid box. Our parameterization keys on the parent GCM's grid-scale diagnosis of dry and moist instability and is discussed in detail by *Levy et al.* [1982, Appendix A] and *Kasibhatla et al.* [1993, section 2]. Being diffusive, it cannot produce inverted vertical profiles of tracers by itself, though the full GCTM has no difficulty doing so (e.g., Figure 7).

In Figures A1 and A2 we evaluate the GCTM's performance in convective situations by comparing with upper tropospheric CO and tropospheric ^{222}Rn data. Figures A1a and A1b compare observed and simulated frequency distributions of CO mixing ratios in the upper troposphere (7.0-11.5 km) over tropical South America during the biomass burning season. The observations were taken over and off the coast of northeastern Brazil during flights 5-7 in TRACE-A [*Fishman et al.*, 1996] and were compared in Figure A1a with simulated CO from the 315 mbar layer in region 29 (see Figure 4) during September and October and in Figure A1b with a single grid box over tropical Brazil during October. The GCTM's CO simulation (see *Kasibhatla et al.* [1996, section 3.2] and T. Holloway et al. (The global distribution of CO, submitted to *Journal of Geophysical Research*, 1999 (hereinafter referred to as submitted paper) for details) employed sources from fossil fuel (300 Tg CO/yr), biomass burning (748 Tg CO/yr), biogenic hydrocarbons (683 Tg CO/yr), and methane

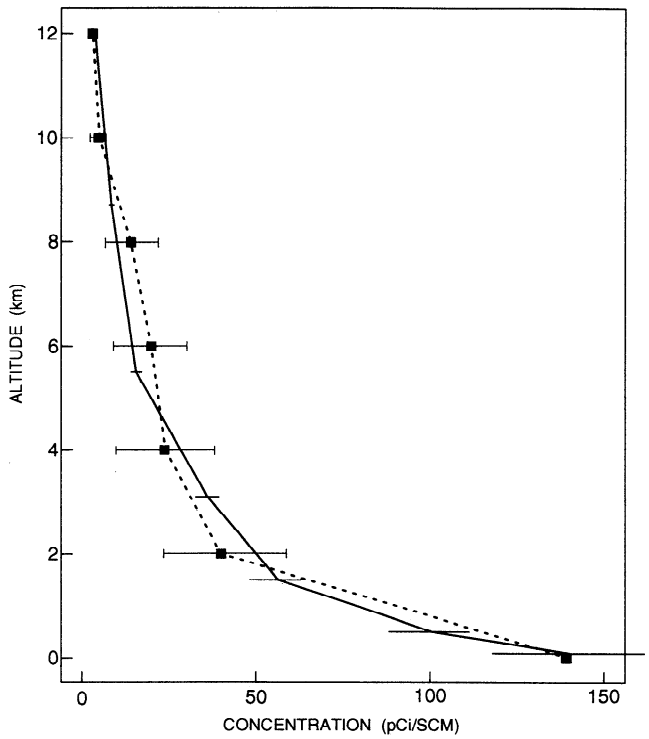

Figure A2. Radon 222 (pCi/scm) in the atmosphere over the central United States. The solid squares are averages of multiple observations, and the brackets represent one standard deviation. The solid line is the area-averaged July mean (35°N-47°N; 80°W-100°W) values from the GCTM, and the horizontal bars indicate one standard deviation of monthly mean model data within the above region.

oxidation (659 Tg CO/yr), had CO destruction driven by the OH fields of *Spivakovsky et al.* [1990], and agreed well (91% of 132 seasonal comparisons with the CMDL flask network within ±25%) with available observations (*T. Holloway et al.*, submitted paper, 1999).

Both the observed and simulated upper tropospheric CO distributions are dominated by the tropical upper tropospheric background with a smaller contribution (~20%) from the continental tropical BL. The simulated background distribution is significantly broader than observed, most likely due to the model's subgrid-scale diffusion, and only the individual grid box over the convective region produces a secondary frequency maximum representative of the BL values. However, the observed secondary maximum is itself the result of nonrandom flights in the vicinity of convective towers over Brazil. While our instability-driven diffusion may not capture the correct physical behavior of an individual convective element, it does appear to capture the basic ensemble behavior over both a single grid box and the larger region of northeastern Brazil. We believe that the upper tropospheric frequency distributions of trace gases such as CO are an excellent tool for evaluating any parameterization of convective transport, including more detailed and explicit parameterizations such as the mass flux approach described by *Allen et al.* [1997].

In Figure A2 we compare simulated ^{222}Rn (surface emissions specified according to *Jacob and Prather* [1990]) with the observed [*Liu et al.*, 1984] summertime ^{222}Rn profile over the central United States (S.-M. Fan, private communication, 1997). The GCTM quantitatively reproduces the observed vertical distribution of ^{222}Rn in a region that is strongly influenced by deep convection. A more detailed discussion of GCTM intercomparisons using ^{222}Rn over continents can be found in the work by *Jacob et al.* [1997, section 3]. Based on Figures A1a, A1b, and A2, we argue that stability-dependent vertical diffusion is quite capable of realistically representing the contribution of convective clouds to vertical transport in a GCTM grid box that is 265 km on a side.

The daily turbulent and convective mixing in the BL is another major challenge for GCTM's. While our convective parameterization will produce episodic BL mixing on a synoptic timescale, it neglects the daily BL mixing observed even during midlatitude winter. Therefore our model's boundary layer is mixed by an additional vertical diffusion that is proportional to the resolved vertical wind shear and that has the same height-dependent mixing lengths as the parent GCM [see *Levy and Moxim*, 1989, section 2.1]. Based on observed tracer profiles in the wintertime continental BL, when instability based mixing is minimal, the GCM's BL mixing lengths have been scaled by 0.5 in the GCTM [*Kasibhatla et al.*, 1993].

Our scale-selective horizontal diffusion, which allows us to retain continental-scale variability while mixing on the small scales, is discussed in detail by *Mahlman and Moxim* [1978, section 3] and *Levy et al.* [1982a,b, Appendix A.2]. The explicit correction of negative mixing ratios, which are generally produced upstream of sharp gradients by numerical advection error, employs mass-conserving downstream borrowing and is essentially diffusive (see *Mahlman and Moxim* [1978] for details).

A3. Deposition

Dry deposition of NO_x and PAN over land, and of HNO_3 over land, oceans, ice, and snow is calculated on the assumption of a balance between surface deposition and the turbulent flux in the bottom half of the lowest model level (for details, see *Levy et al.* [1985, section 2.3], *Levy and Moxim* [1989, section 2.4], and *Kasibhatla et al.* [1993, equation (2.2)]). The individual deposition velocities (w_d) are given in Table A1. We assume that particulate NO_3^- is the major component of soluble nitrogen over the ocean (see *Kasibhatla et al.* [1993, section 3, and references therein] for details).

Our wet removal scheme (see *Kasibhatla et al.* [1991, section 2 and equations (1)-(3)] for details) distinguishes between stable or shallow-convective precipitating clouds (liquid water content assumed to be 0.5×10^{-6} g cm^{-3} [*Giorgi and Chameides*, 1986]) and deep convective precipitating clouds (liquid water content assumed to be 2.0×10^{-6} g cm^{-3} [*Giorgi and Chameides*, 1986]) and only removes the highly soluble tracer, HNO_3. The fraction of HNO_3 removed from the grid box each time step is equal to the fraction of the precipitating grid volume filled by cloud liquid water. The numerator of this fraction is the grid box's portion of the total column precipitation divided by the appropriate liquid water content and the denominator is the volume of the grid box. As in the parent GCM, we assume a precipitation efficiency of 100% for cloud water. In a sensitivity test, *Kasibhatla et al.* [1993] found that a 50% reduction in this effective first-order removal coefficient (1) reduced HNO_3 wet deposition by 20-30% in source regions with less impact downwind and at remote locations; (2) did not affect NO_x levels in source regions, though NO_x levels did increase slightly in remote regions.

Table A1. Dry Deposition Velocities for HNO_3, NO_x, and PAN

Tracer	Snow or Ice	Water	Land With T_{11}>10°C	Land With T_{11}< -10°C	Land for -10°C<T_{11}<10°C
HNO_3	0.5	0.3	1.5	same as snow and ice	linear interpolation between 10°C and -10°C
NO_x	0	0	0.25	0	same as above
PAN	0	0	0.25	0	same as above

Values are in units of cm/s.

A4. NO_x Emissions

The emissions from fossil fuel combustion (22.4 TgN/yr) are constructed from the Global Emissions Inventory Activity (GEIA) 1990 seasonally varying source function. This source, which corresponds to 1985 fossil fuel emission levels, was extrapolated to 1990 levels using energy data from the *U.S. Energy Information Administration* (EIA) [1997; J. Yienger, personal communication, 1998], and the Asian emissions were replaced by the RAINS-Asia 1990 emissions inventory of *van Aardenne et al.* [1999]. The global distribution is similar to that shown in Figures 1 of *Levy and Moxim* [1989a,b] and *Kasibhatla et al.* [1993], though the source magnitude has increased in Asia, decreased slightly in North America, and increased slightly in Europe. These emissions are partitioned into a surface flux, representing emissions from transportation, and volume sources in the lowest two levels, representing emissions from short and tall (> 100 m) stacks, respectively (see *Levy and Moxim* [1989a, section 2.2] for a detailed discussion of the source partitioning among the three categories).

The annual biomass burning source of 7.8 TgN/yr (see *Levy et al.* [1991, Figure 43.1] for the spatial pattern of the source and *M.K. Galanter et al.*, submitted paper, 1999 for details) is emitted as a surface flux. The previous estimate of 8.5 Tg N/yr [*Levy et al.*, 1991] has been reduced by 0.7 Tg N/yr because of a 30% reduction in the emissions from the savannas of northern Africa based on recent measurements of NO_x/CO_2 ratios in the Ivory Coast (0.0014 [*Delmas et al.*, 1995]) as well as the removal of all high-altitude emissions from the Andes (GCTM altitude >2.5 km). The source reflects emissions from six biomass types: forest, savanna, fuelwood, agricultural residues, domestic crop residues, and animal waste. It is constructed from a gridded 1°x1° CO biomass burning source (J. Logan, personal communication, 1990) and converted to an NO_x source using field and laboratory measurements of emission ratios for CO/CO_2 (0.08 [*Andrea et al.*, 1988]) and NO_x/CO_2 (0.002 [*Hao et al.*, 1990]).

The tropical rainforests and subtropical savannas of Africa, South and Central America, Asia, and Australia were divided into 20 regions, based on broad similarities in vegetation, cultural patterns, cultivation practices, and climate. For each region the period of burning and the monthly fraction of emissions from forests and savannas were determined based on cultural and agricultural practices and satellite observations [*Richardson*, 1994; J.R. Olson, personal communication, 1998; M.K. Galanter et al., submitted paper, 1999, Table 2]. In Asia, NO_x emissions from biofuel combustion (domestic crop residues and dung) and fuelwood are based on *Streets and Waldhoff* [1998], and elsewhere in the tropics, the fraction of emissions from fuelwood and agricultural residues is based on *Hao and Liu* [1994]. Fuelwood and biofuels are assumed to be burned year-round, while agricultural residue has the same timing as tropical forests and savannas. Poleward of 35°, emissions from biomass burning are based on the original 1°x1° CO biomass burning source and are released only in the summer months.

The time-dependent soil-biogenic emissions (5 TgN/yr) are given by a temperature and precipitation dependent, empirically based, source function that is driven by 6-hour GCM forcing (see *Yienger and Levy* [1995] for a detailed discussion of the algorithm and see their Figure 1 for global maps of the annual emissions). The source function includes synoptic-scale modeling of "pulsing" (the emissions burst following the wetting of a dry soil) which contributes ~1.3 Tg N annually; a biome-dependent scheme to estimate canopy recapture of NO_x; and an explicit linear dependence of emission on N-fertilizer rate for present agricultural soils. As a result of recent measurements of very low soil nitrate levels and NO_x soil-biogenic emissions in the wet Savannas of the Ivory Coast [*Le Roux et al.*, 1995], we have reduced the emission rates from the savannas of northern Africa to ~10% of the published value. Our best estimate of present, above-canopy emissions is now 5.0 Tg N (NO_x) with agriculture, primarily in the extratropics, and grasslands, primarily in the tropics, accounting for 45% and 30%, respectively. Tropical rain forests account for most of the remainder (17%).

The horizontal and temporal distribution for our lightning source of NO_x is constructed from the parent GCM's deep moist convection statistics. NO_x is emitted when deep moist convective instability is diagnosed, which directly couples the emissions to both large-scale upward transport and strong vertical mixing in the column. The source distribution also employs observations of cloud-to-ground and cloud-to-cloud lightning fractions, the observed vertical distribution of lightning discharge [*Proctor*, 1991], and empirical/theoretical estimates of relative lightning frequency resulting from deep moist convection over ocean and over land [*Price and Rind*, 1992]. The vertical distribution of the source is given by *Levy et al.* [1996, Figure 3]. By comparing our GCTM simulations of tropospheric NO_x with measurements of NO_x and/or NO_y in the middle and upper troposphere where lightning is a major, if not the dominant, source, we are able to bracket the global NO_x emissions between 2 and 6 TgN/yr. For this study the global source is assumed to be 4 TgN/yr (see *Levy et al.* [1996] for a detailed discussion of the source development and their Figure 2 for the global emission pattern). While lower than the recent *Price et al.* [1997] calculation of 12 TgN/yr based on a GCM analysis, our value is consistent with the reanalysis of *Lawrence et al.* [1995] and the recent laboratory studies of *Wang et al.* [1998a]. As previously noted by *Levy et al.* [1996], the scaled global source strength, though not the temporal and spatial distributions, depends critically on the GCTM's OH fields. This issue is discussed in section 5.

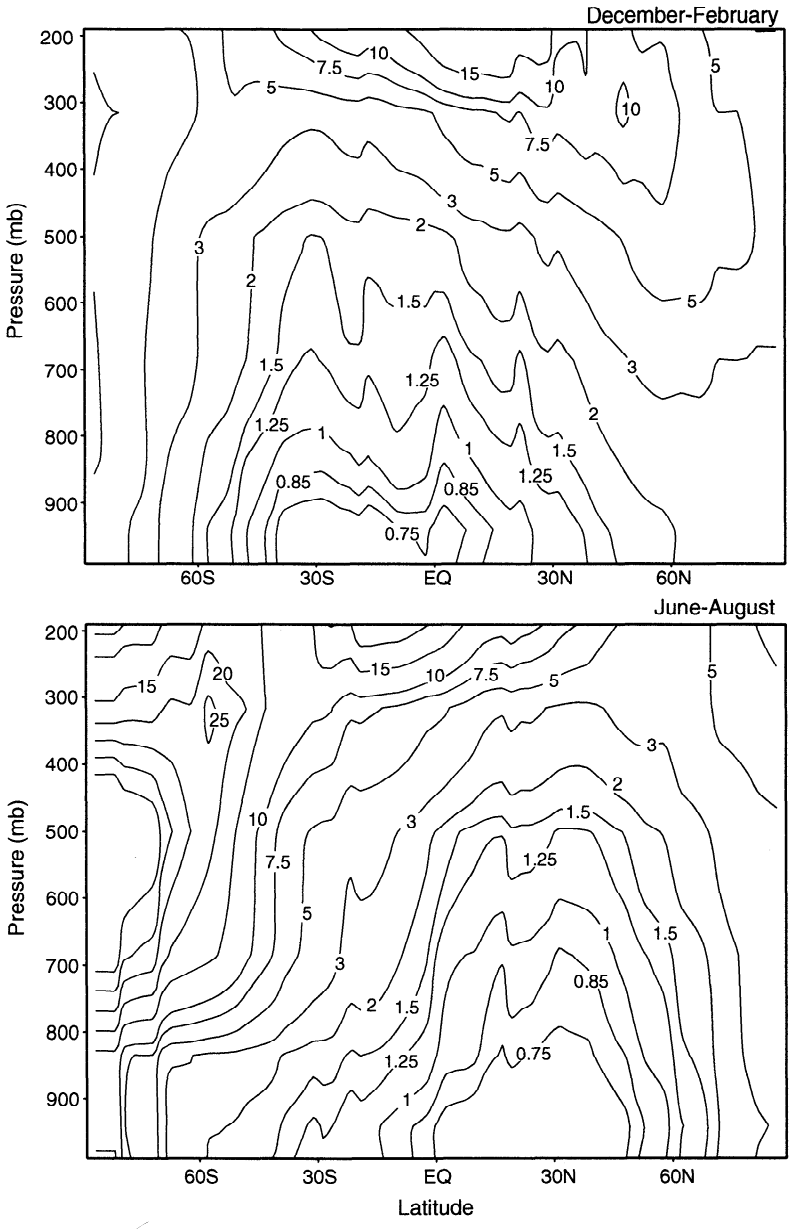

Figure A3. Zonal average NO_x to HNO_3 conversion times based on the gas phase OH reaction plus the nighttime heterogeneous conversion via NO_3 and N_2O_5 for winter (December - February) and summer (June - August).

We use zonally and monthly averaged O_3 and N_2O fields to calculate the present production of NO in the stratosphere from the oxidation of N_2O by $O(^1D)$ (see *Kasibhatla et al.* [1991] for details) with a maximum rate of 200-240 molecules/cm^3/s. The zonal distribution of the annual-average source is shown in the work by K*asibhatla et al.* [1991, Figure 2]. While NO is produced continuously in the stratosphere, it is injected episodically as a collection of NO_y species into the troposphere, particularly during the winter and spring at middle and high latitudes. The 3-D time-independent emission of NO_x by aircraft occurs primarily in the upper troposphere of the middle and high latitudes of the NH and has a magnitude of 0.45 TgN/yr (see *Kasibhatla* [1993] and references therein for details).

For this study, we neglect a hypothesized NO_x sink, loss via reactions with ammonia (~1 Tg/yr [*Dentener and Crutzen*, 1994]), and a proposed source of emissions from higher plant species (<0.2 Tg/yr [*Wildt et al.*, 1997]). These two processes, which are uncertain and small relative to uncertainties in the sources included in our study, should have negligible impact on either our NO_x simulations or the subsequent analysis and conclusions. The only ship emissions included are those from European and Asian shipping, and they have all been consolidated in the nearest coastal grid boxes.

A5. Chemistry

Effective first-order rate coefficients for the chemical interconversions among NO_x, HNO_3, and PAN are interpolated from monthly mean, zonally averaged tables carried in the GCTM. PAN formation occurs via the reaction of peroxyacetyl radical (PAC) with NO_2. The PAC is generated by the reaction of nonmethane hydrocarbons (NMHC) (2-D monthly

varying ethane and propane fields from *Kanakidou et al.* [1991]) with OH (see *Kasibhatla et al.* [1991, section 3] for details). Over continents, short-lived natural hydrocarbons, such as isoprene, can contribute significantly to PAN formation [e.g., *Trainer et al.*, 1991; *Horowitz et al.*, 1998]. To approximately reproduce observed summer PAN levels at a rural site in the eastern United States (Scotia, Pennsylvania), as well as PAN fractions measured during periods of east winds at Boulder, Colorado, in February (M. P. Buhr, private communication, 1992), and at Egbert, Ontario, in April [*Shepson et al.*, 1991], we have increased NMHC concentrations over land in the bottom three model levels between 30°N and 65°N by a factor of 3 in summer and by a factor of 1.5 in spring and fall, relative to the 2-D fields of *Kanakidou et al.* [1991]. South of 30°N, NMHC concentrations over land in the bottom three model levels have been adjusted so that, throughout the year, they are approximately equal to summer, lower tropospheric NMHC concentrations over land specified between 30°N and 65°N. This is based on studies [e.g., *Chameides et al.*, 1992] which find that, on an OH reactivity based scale, surface hydrocarbon levels observed over remote tropical forests are comparable to those in the rural areas of the eastern United States during summer.The thermal decomposition rate of PAN is calculated on-line as a function of the local model temperature. Detailed discussions of the gas phase chemistry used in this study are given by *Kasibhatla et al.* [1991, section 2 and appendix], *Kasibhatla et al.* [1993, section 2], and *Moxim et al.* [1996, section 2].

The GCTM's OH fields give a global CH_3CCl_3 lifetime of 6.3 years, which is in reasonable agreement with 5.5 years calculated by *Spivakovsky et al.*[1990] and 6.2 years inferred from CH_3CCl_3 observations [*Prinn et al.*, 1987]. Recently, acetone has been proposed as a major source of upper tropospheric HO_x [*Singh et al.*, 1995], and the estimated CH_3CCl_3 lifetime has been reduced to 4.8 years [*Prinn et al.*, 1995]. These two developments would support a 25-30% increase in global OH and up to a 50% increase in OH in the upper troposphere, with related decreases in the chemical lifetime of NO_x [*Klonecki*, 1998]. In section 5 we examine the possible impacts of these modifications on our simulation and analyses.

The nighttime first-order rate coefficients for heterogeneous conversion of NO_2 to HNO_3 on sulfate aerosol via NO_3 and N_2O_5 are calculated off-line and carried as monthly average 3-D fields. Using monthly average 10°x10° fields of the first-order rate coefficient for N_2O_5 loss on sulfate aerosols [*Dentener and Crutzen*, 1993], local model temperatures, and the same 2-D ozone and NO_x fields used in the gas phase chemistry, we integrate the time-dependent nighttime chemical equations for NO_2, NO_3, and N_2O_5 for each 10°x10° grid box. A 1 hour lifetime for the removal of NO_3 by reaction with either dimethyl sulfide (DMS) or alkenes is used in the model's BL. We assume that all of the nitrogen oxides are in the form of NO_2 at sunset and integrate the equations until sunrise. The nighttime reductions in total nitrogen oxides (NO_2(sunset) - NO_2(sunrise) - NO_3 (sunrise) - N_2O_5(sunrise)) are then converted into first-order rate coefficients for the heterogeneous conversion of NO_2 to HNO_3, linearly interpolated to the GCTM's grid, and carried as monthly average 3-D tables of heterogeneous conversion of NO_x to HNO_3.

In Figure A3 we plot the GCTM's zonal average DJF and JJA NO_x chemical lifetimes due to the gas phase oxidation of NO_x to HNO_3 by OH and the heterogeneous nighttime conversion via NO_3 and N_2O_5. The NO_x chemical lifetimes in the BL and lower troposphere range from 0.75-1.0 days in the tropics and summer midlatitudes, where gas phase chemistry dominates, to 1-3 days in the winter midlatitudes and the polar regions, where nighttime heterogeneous chemistry is in control. The NO_x lifetime increases with height, reaching 5-10 days in the upper troposphere, due to the decrease in H_2O and temperature. Throughout the lower half of the troposphere, the lifetime minimum follows the Sun. The dip in the subtropical lower troposphere during each hemisphere's summer results from an OH minimum, while the bump in the subtropical lower troposphere during each hemisphere's winter results from the addition of two processes with sharp and opposing gradients. Gas phase oxidation is generally in control, with nighttime heterogeneous oxidation only dominating at high latitudes during the winter, where sunlight and OH are either absent or very low. While the gas phase temperature-sensitive oxidation of NO_x to NO_3 is generally the rate-controlling step for heterogeneous oxidation, it is more complex in the southern high latitudes, where low temperatures, low O_3, and much lower sulfate aerosol levels result in longer wintertime NO_x lifetimes. The decrease in NO_x lifetimes in the high-latitude lower stratosphere is driven by the much higher levels of O_3. A detailed discussion of the potential uncertainties in our treatment of chemistry, and its impact on both our simulated NO_x and the associated analysis of source impacts, are given in section 5.

Acknowledgments. We wish to thank James J. Yienger for developing the updated fossil fuel combustion source, Meredith K. Galanter for developing the updated biomass burning source, and Song-Miao Fan for his analysis of the transport behavior of the GCTM. We gratefully acknowledge the merged data sets provided by the Georgia Institute of Technology with the financial aid of NASA's SASS and GTE research programs; we wish to individually thank J. Crawford, B. Ridley, J. Walega, S. Sandholm, and the late John Bradshaw for providing additional measurement data; and we wish to thank A.I. Hirsch for initially gathering and processing much of the measurement data. We wish to thank C. Andronache and J.D. Mahlman for their careful reading of the manuscript and for their helpful comments, and we wish to acknowledge the thoughtful and helpful comments of two anonymous reviewers. One of us (P.S.K.) was funded by the Atmospheric Chemistry Project of the NOAA Climate and Global Change Program under grant NA36GP0250 and by the National Science Foundation under grant ATM-9213643, and one of us (A.A.K.) wishes to acknowledge support from NASA grant NGT 5-30015.A01.

References

Allen, D. J., K. E. Pickering, and A. Molod, An evaluation of deep convective mixing in the Goddard Chemical Transport Model using International Satellite Cloud Climatology Project cloud parameters, *J. Geophys. Res., 102,* 25,467-25,476, 1997.

Andrea, M. O., et al., Biomass-burning emissions and associated haze layers over Amazonia, *J. Geophys. Res., 93,* 1509 - 1527, 1988.

Atlas, E., and B. A. Ridley, The Mauna Loa Observatory photochemistry experiment: Introduction, *J. Geophys. Res., 101,* 14,531-14,541, 1996.

Benkovitz, C. M., J. Dignon, J. Pacyna, T. Scholtz, L. Tarrason, E. M. Voldner, and T.E. Graedel, Global gridded inventories of anthropogenic emissions of SO_2 and NO_x, *J. Geophys. Res., 101,* 29,239-29,254, 1996.

Bradshaw, J., S. Sandholm, and R. Talbot, An update on reactive odd-nitrogen measurements made during recent NASA Global Tropospheric Experiment programs, *J. Geophys. Res., 103,* 19,129-19,148, 1998.

Bradshaw, J., et al., Photofragmentation two-photon laser-induced fluorescence detection of NO_2 and NO: Comparison of measurements with model results based on airborne observations during PEM-Tropics A, *Geophys. Res. Lett., 26*, 471-474, 1999.

Brasseur, G. P., D. A. Hauglustaine, and S. Walters, Chemical compounds in the remote Pacific troposphere: Comparisons between MLOPEX measurements and chemical transport model calculations, *J. Geophys. Res., 101*, 14,795-14,813, 1996.

Carroll, M. A., and A. M. Thompson, NO_x in the non-urban troposphere, in *Progress and Problems in Atmospheric Chemistry*, edited by J.R. Barker, World Sci., River Edge, N.J., 1995.

Carroll, M. A., D. D. Montzka, G. Hubler, K. K. Kelly, and G. L. Gregory, In situ measurements of NO_x in the Airborne Arctic Stratospheric Expedition, *Geophys. Res. Lett., 17*, 493-496, 1990.

Carsey, T. P., et al., Nitrogen oxides and ozone production in the North Atlantic marine boundary layer, *J. Geophys. Res., 102*, 10,653-10,665, 1997.

Chameides, W. L., and A. Tan, The two-dimensional diagnostic model for tropospheric OH: An uncertainty analysis, *J. Geophys. Res., 86*, 5209-5223, 1981.

Chameides, W. L., and J. C. G. Walker, A photochemical theory of tropospheric ozone, *J. Geophys. Res., 78*, 8751-8760, 1973.

Chameides, W. L., D. D. Davis, M. O. Rogers, J. Bradshaw, and S. Sandholm, Net ozone photochemical production over the eastern and central North Pacific as inferred from GTE/CITE 1 observations during fall 1983, *J. Geophys. Res., 92*, 2131-2152, 1987.

Chameides, W. L., et al., Ozone precursor relationships in the ambient atmosphere, *J. Geophys. Res., 97*, 6037-6055, 1992.

Chameides, W. L., P. S. Kasibhatla, J. J. Yienger, H. Levy II, and W. J. Moxim, The growth of continental-scale metro-agro-plexes, regional ozone pollution, and world food production, *Science, 264*, 74-77, 1994.

Chatfield, R. B., and P. J. Crutzen, Sulfur dioxide in remote oceanic air: Cloud transport of reactive precursors, *J. Geophys. Res., 89*, 7111-7132, 1984.

Crawford J., et al., Photostationary state analysis of the NO_2-NO system based on airborne observations from the western and central North Pacific, *J. Geophys. Res., 101*, 2053-2072, 1996.

Crosley, D. R., NO_y Blue Ribbon panel, *J. Geophys. Res., 101*, 2049-2052, 1996.

Crutzen, P. J., Photochemical reaction initiated by and influencing ozone in unpolluted tropospheric air, *Tellus, 26*, 45 - 55, 1974.

Crutzen, P. J., The role of NO and NO_2 in the chemistry of the troposphere and stratosphere, *Annu. Rev. Earth Planet. Sci., 7*, 443-472, 1979.

Delmas, R., J. P. Lacaux, J. C. Menaut, L. Abbadie, X. Le Roux, G. Helas, and J. Lobert, Nitrogen compound emission from biomass burning in tropical African savanna FOS/DECAFE 1991 Experiment (Lamto, Ivory Coast), *J. Atmos. Chem., 22*, 175-193, 1995.

Denning, A. S., et al., Three-dimensional transport and concentration of SF6. A model intercomparison study (TransCom 2), *Tellus, Ser. B, 51*, 266-297, 1999.

Dentener, F. J., and P. J. Crutzen, Reaction of N_2O_5 on tropospheric aerosols: Impact on the global distribution of NO_x, O_3, and OH, *J. Geophys. Res., 98*, 7149-7163, 1993.

Dentener, F. J., and P. J. Crutzen, A three-dimensional model of the global ammonia cycle, *J. Atmos. Chem., 19*, 331-369, 1994.

Emmons, L. K., et al., Climatologies of NO_x and NO_y: A comparison of data and models, *Atmos. Environ., 31*, 1851-1904, 1997.

Fishman, J., S. Solomon, and P. J. Crutzen, Observational and theoretical evidence in support of a significant in-situ photochemical source of tropospheric ozone, *Tellus, 31*, 432-446, 1979.

Fishman, J., C. E. Watson, J. C. Larsen, and J. A. Logan, Distribution of tropospheric ozone determined from satellite data, *J. Geophys. Res., 95*, 3599-3617, 1990.

Fishman, J., J. M. Hoell Jr., R. D. Bendura, R. J. McNeal, and V. W. J. H. Kirchhoff, NASA GTE TRACE-A experiment (September-October 1992): Overview, *J. Geophys. Res., 101*, 23,865-23,879, 1996.

Friedl, R. (Ed.), Atmospheric effects of subsonic aircraft:interim assessment report of the advanced subsonic Technology Program, *NASA Ref. Publ., 1400*, May 1997.

Galloway, J. N., H. Levy II, and P. S. Kasibhatla, Year 2020: Consequences of population growth and development on deposition of oxidized nitrogen, *Ambio, 23*, 120-123, 1994.

Galloway, J. N., W. H. Schlesinger, H. Levy II, A. Michaels, and J.L. Schnoor, Nitrogen fixation: Anthropogenic enhancement-environmental response, *Global Biogeochem. Cycles, 9*, 235-252,1995.

Giorgi, F., and W. L. Chameides, Rainout lifetimes of highly soluble aerosols and gases as inferred from simulations with a general circulation model, *J. Geophys. Res., 91*, 14,367-14,376, 1986.

GLOBALVIEW-CO2, Cooperative atmospheric data integration project - Carbon dioxide, NOAA Climate Monitoring and Diagnostics Lab., Boulder, Colo., 1996.

Hao, W. M., and M.-H. Liu, Spatial and temporal distribution of tropical biomass burning, *Global Biogeochem. Cycles*, 8, 495-603, 1994.

Hao, W. M., M.-H. Liu, and P. J. Crutzen, Estimates of annual and regional releases of CO_2 and other trace gases to the atmosphere from fires in the tropics, based on FAO statistics for the period 1975-1980, in *Fire in the Tropical Biota, Ecol. Stud.*, vol. 84, edited by J.G. Goldammer, pp. 440-462, Springer-Verlag, New York, 1990.

Harriss, R. C., et al., The Amazon Boundary Layer Experiment (ABLE-2A): Dry season 1985, *J. Geophys. Res., 93*, 1351-1360, 1988.

Harriss, R. C., et al., The Amazon Boundary Layer Experiment: Wet season 1987, *J. Geophys. Res., 95*, 16,721-16,736, 1990.

Harriss, R. C., et al., The Arctic Boundary Layer Expedition (ABLE 3A): July-August 1988, *J. Geophys. Res., 97*, 16,383-16,394, 1992.

Harriss, R. C., S. C. Wofsy, J. M. Hoell Jr., R. J. Bendura, J. W. Drewry, R. J. McNeal, D. Pierce, V. Rabine, and R. L. Snell, The Arctic Boundary Layer Expedition (ABLE 3B), July-August 1990, *J.Geophys. Res., 99*, 1635-1644, 1994.

Hauglustaine, D. A., S. Madronich, B. A. Ridley, J. G. Walega, C. A. Cantrell, R. E. Shetter, and G. Hubler, Observed and model-calculated photostationary state at Mauna Loa Observatory during MLOPEX 2, *J. Geophys. Res., 101*, 14,681-14,696, 1996a.

Hauglustaine, D. A., B. A. Ridley, S. Solomon, P. G. Hess, and S. Madronich, HNO_3/NO_x ratio in the remote troposphere during MLOPEX 2: Evidence for nitric acid reduction on carbonaceous aerosols, *Geophys. Res. Lett., 23*, 2609-2612, 1996b.

Hjellbrekke, A.-G., J. Schaug, and J. E. Skjelmoen, EMEP data report 1994, *EMEP/CCC 4/96*, Kjeller, Norway, 1996.

Hoell, J. M., Jr., D. L. Albritton, G. L. Gregory, R. J. McNeal, S. M. Beck, R. J. Bendura, and J. W. Drewry, Operational overview of NASA GTE/CITE 2 airborne instrument intercomparisons: Nitrogen dioxide, nitric acid, and peroxyacetyl nitrate. *J. Geophys. Res., 95*, 10,047-10,054, 1990.

Hoell, J. M., Jr., et al., Operational overview of the NASA GTE/CITE3 airborne instrument intercomparisons for sulfur dioxide, hydrogen sulfide, carbonyl sulfide, dimethyl sulfide, and carbon disulfide, *J. Geophys. Res., 98*, 23,291-23,304, 1993.

Hoell, J. M., D. D. Davis, S. C. Liu, R. E. Newell, M. Shipham, H. Akimoto, R. J. McNeal, R. J. Bendura, and J. W. Drewry, Pacific Exploratory Mission West-A(PEM West-A): September-October 1991, *J. Geophys. Res., 101*, 1641-1653, 1996.

Hoell, J. M., D. D. Davis, S. C. Liu, R. E. Newell, H. Akimoto, R. J. McNeal, and R. J. Bendura, The Pacific Exploratory Mission-West Phase B: February-March 1994, *J. Geophys. Res., 102*, 28,223-28,240, 1997.

Hoell, J. M., D. D. Davis, D. J. Jacob, M. O. Rogers, R. E. Newell, H. E. Fuelberg, R. J. McNeal, J. L. Raper, and R. J. Bendura, Pacific Exploratory Mission in the tropical Pacific: PEM-Tropics A, August-September 1996, *J. Geophys Res., 104*, 5567-5584, 1999.

Horowitz, L. W., J. Liang, G. M. Gardner, and D. J. Jacob, Export of reactive nitrogen from North America during summertime: Sensitivity to hydrocarbon chemistry, *J. Geophys. Res., 103*, 13,451-13,476, 1998.

Jacob, D. J., and M. J. Prather, Radon-222 as a test of boundary layer convection in a general circulation model, *Tellus, Ser. B, 42*, 118-134, 1990.

Jacob, D. J., M. J. Prather, S. C. Wofsy, and M. B. McElroy, Atmo-

spheric distribution of Kr85 simulated with a general circulation model, *J. Geophys. Res., 92,* 6614-6626, 1987.

Jacob, D. J., et al., Origin of ozone and NO_x in the tropical troposphere: A photochemical analysis of aircraft observations over the South Atlantic basin, *J. Geophys. Res., 101,* 24,235-24,250, 1996.

Jacob, D. J., et al., Evaluation and intercomparison of global atmospheric transport models using ^{222}Rn and other short-lived tracers, *J. Geophys. Res., 102,* 5953-5970, 1997.

Jaegle, L., et al., Observations of OH and HO_2 in the upper troposphere suggest a strong source from convective injection of peroxides, *Geophys. Res. Lett., 24,* 3181-3184, 1997.

Jaffe, D. A., T. K. Bernsten, and I. S. A. Isaksen, A global three-dimensional chemical transport model, 2, Nitrogen oxides and non-methane hydrocarbon results, *J. Geophys. Res., 102,* 21,281-21,296, 1997.

Kanakidou, M., H. B. Singh, K. M. Valentin, and P. J. Crutzen, A two-dimensional study of ethane and propane oxidation in the troposphere, *J. Geophys. Res., 96,* 15,395-15,425, 1991.

Kasibhatla, P. S., NO_y from subsonic aircraft emissions: A global three-dimensional model study, *Geophys. Res. Lett., 20,* 1707-1710, 1993.

Kasibhatla, P. S., H. Levy II, W. J. Moxim, and W. L. Chameides, The relative impact of stratospheric photochemical production on tropospheric NO_y levels: A model study, *J. Geophys. Res., 96,* 18,631-18,646, 1991.

Kasibhatla, P. S., H. Levy II, and W. J. Moxim, Global NO_x, HNO_3, PAN and NO distributions from fossil-fuel combustion emissions: A model study, *J. Geophys. Res., 98,* 7165-7180, 1993.

Kasibhatla, P. S., H. Levy II, A. A. Klonecki, and W. L. Chameides, A three-dimensional view of the large-scale tropospheric ozone distribution over the North Atlantic Ocean during summer, *J. Geophys. Res., 101,* 29,305-29,316, 1996.

Kawakami, S., et al., Impact of lightning and convection on reactive nitrogen in the tropical free troposphere, *J. Geophys. Res., 102,* 28,367-28,384, 1997.

Klonecki, A. A., Model study of the tropospheric chemistry of ozone, Ph.D. thesis, Princeton Univ., Princeton, N.J., 1998.

Klonecki, A. A., and H. Levy II, Tropospheric chemical ozone tendencies in the $CO\text{-}CH_4\text{-}NO_y\text{-}H_2O$ system: Their sensitivity to variations in environmental parameters and their application to a GCTM study, *J. Geophys. Res., 102,* 21,221-21,237, 1997.

Kraus, A. B., F. Rohrer, E. S. Grobler, and D. H. Ehhalt, The global tropospheric distribution of NO_x estimated by a three-dimensional chemical tracer model, *J. Geophys. Res., 101,* 18,587-18,604, 1996.

Lacaux, C. G., and A. I. Modi, Precipitation chemistry in the Sahelian savanna of Niger, Africa, *J. Atmos. Chem., 30,* 319-343, 1998.

Lamarque, J.-F., G. P. Brasseur, P. G. Hess, and J.-F. Muller, Three-dimensional study of the relative contributions of the different nitrogen sources in the troposphere, *J. Geophys. Res., 101,* 22,955-22,968, 1996.

Lawrence, M. G., W. L. Chameides, P. S. Kasibhatla, H. Levy II, and W. Moxim, Lightning and atmospheric chemistry, in *The Rate of Atmospheric NO Production, Handbook of Atmos. Electrodyn.*, vol. 1, edited by H. Volland, pp. 189-202, CRC Press, Boca Raton, Fla., 1995.

Le Roux, X., L. Abbadie, R. Lensi, and D. Serca, Emission of nitrogen monoxide from African tropical ecosystems: Control of emission by soil characteristics in humid and dry savannas of West Africa, *J. Geophys. Res., 100,* 23,133-23,142, 1995.

Levy, H., II, Normal atmosphere: Large radical and formaldehyde concentrations predicted, *Science, 173,* 141 - 143, 1971.

Levy, H., II, and W. J. Moxim, Simulated global distribution and deposition of reactive nitrogen emitted by fossil fuel combustion, *Tellus, 41,* 256-271, 1989a.

Levy, H., II, and W. J. Moxim, Influence of long-range transport of combustion emissions on the chemical variability of the background atmosphere, *Nature, 338,* 326-328, 1989b.

Levy, H., II, J. D. Mahlman, and W. J. Moxim, A preliminary report on the numerical simulation of the three-dimensional structure and variability of atmospheric N_2O, *Geophys. Res. Lett., 6,* 155-158, 1979.

Levy, H., II, J. D. Mahlman, and W. J. Moxim, Tropospheric N_2O variability, *J. Geophys. Res., 87,* 3061-3080, 1982.

Levy, H., II, J. D. Mahlman, W. J. Moxim, and S. C. Liu, Tropospheric ozone: The role of transport, *J. Geophys. Res., 90,* 3753-3772, 1985.

Levy, H., II, W. J. Moxim, P. S. Kasibhatla, and J. A. Logan, The global impact of biomass burning on tropospheric reactive nitrogen, in *Global Biomass Burning: Atmospheric, Climatic, and Biospheric Implications*, edited by J. S. Levine, pp. 363-369, MIT Press, Cambridge, Mass., 1991.

Levy, H., II, W. J. Moxim, and P. S. Kasibhatla, Impact of global NO_x sources on the northern latitudes, in *The Tropospheric Chemistry of Ozone in Polar Regions, NATO ASI Ser.,* vol. 17, edited by H. Niki and K. H. Becker, pp. 77-88, Springer-Verlag, New York, 1993.

Levy, H., II, W. J. Moxim, and P. S. Kasibhatla, Global three-dimensional time-dependent lightning source of tropospheric NO_x, *J. Geophys. Res., 101,* 22,911-22,922, 1996.

Levy II, H., P. S. Kasibhatla, W. J. Moxim, A. A. Klonecki, A. I. Hirsch, S. J. Oltmans, and W. L. Chameides, The global impact of human activity on tropospheric ozone, *Geophys. Res. Lett., 24,* 791-794, 1997.

Lin, X., M. Trainer, and S. C. Liu, On the nonlinearity of the tropospheric ozone production, *J. Geophys. Res., 93,* 15,879-15,888, 1988.

Liu, S. C., M. McFarland, D. Kley, O. Zafiriou, and B. Huebert, Tropospheric NO_x and O_3 budgets in the equatorial Pacific, *J. Geophys. Res., 88,* 1360-1368, 1983.

Liu, S. C., J. R. McAfee, and R. J. Cicerone, Radon 222 and tropospheric vertical transport, *J. Geophys. Res., 89,* 7291-7297, 1984.

Liu, S. C., et al., A study of the photochemistry and ozone budgets during the Mauna Loa Observatory Photochemistry Experiment, *J. Geophys. Res., 97,* 10,463-10,471, 1992.

Logan, J. A., Nitrogen oxides in the troposphere: Global and regional budgets, *J. Geophys. Res., 88,* 10,785-10,807, 1983.

Mahlman, J. D., and W. J. Moxim, Tracer simulation using a global general circulation model: Results from a midlatitude instantaneous source experiment, *J. Atmos. Sci., 35,* 1340-1374, 1978.

Manabe, S., and J. L. Holloway Jr., The seasonal variation of the hydrologic cycle as simulated by a global model of the atmosphere, *J. Geophys. Res., 80,* 1617 - 1649, 1975.

Manabe, S., D. G. Hahn, and J. L. Holloway Jr., The seasonal variation of the tropical circulation as simulated by a global model of the atmosphere, *J. Atmos. Sci., 31,* 43 - 83, 1974.

Merrill, J. T., R. E. Newell, and A. S. Bachmeier, A meteorological overview for the Pacific Exploratory Mission-West Phase B, *J. Geophys. Res., 102,* 28,241-28,254, 1997.

Moxim, W. J., Simulated transport of NO_y to Hawaii during August: A synoptic study, *J. Geophys. Res., 95,* 5717-5729, 1990.

Moxim, W. J., H. Levy II, and P. S. Kasibhatla, Simulated global tropospheric PAN: Its transport and impact on NO_x, *J. Geophys. Res., 101,* 12,621-12,638, 1996.

National Atmospheric Deposition Program (NRSP-3)/National Trends Network, NADP/NTN Program Office, Ill. State Water Surv., Champaign, 1998.

Penner, J. E., C. S. Atherton, J. Dignon, S. J. Ghan, J. J. Walton, and S. Hameed, Tropospheric nitrogen: A three-dimensional study of sources, distributions, and deposition, *J. Geophys. Res., 96,* 959-990, 1991.

Pickering, K. E., et al., Convective transport of biomass burning emissions over Brazil during TRACE A, *J. Geophys. Res., 101,* 23,993-24,012, 1996.

Potter, C. S., J. T. Randerson, C. B. Field, P. A. Matson, P. M. Vitousek, H. A. Mooney, and S. A. Klooster, Terrestrial ecosystem production: A process model based on global satellite and surface data, *Global Biogeochem. Cycles, 7,* 811-841, 1993.

Price, C., and D. Rind, A simple parameterization for calculating global lightning distributions, *J. Geophys. Res., 97,* 9919-9933, 1992.

Price, C., J. Penner, and M. Prather, NO_x from lightning, 1, Global distribution based on lightning physics, *J. Geophys. Res., 102,* 5929-5942, 1997.

Prinn, R. G., D. Cunnold, R. Rasmussen, P. Simmonds, F. Alyea, A. Crawford, P. Fraser, and R. Rosen, Atmospheric trends in methylchloroform and the global average for the hydroxyl radical, *Science, 238*, 945-950, 1987.

Prinn, R. G., R. F. Weiss, B. R. Miller, J. Huang, F. N. Alyea, D. M. Cunnold, P. J. Fraser, D. E. Hartley, and P. G. Simmonds, Atmospheric trends and lifetimes of CH_3CCl_3 and global OH concentrations, *Science, 269*, 187-192, 1995.

Proctor, D. E., Regions where lightning flashes began, *J. Geophys. Res., 96*, 5099 - 5112, 1991.

Richardson, J. L., An investigation of large-scale tropical biomass burning and the impact of its emissions on atmospheric chemistry, Ph.D. thesis, Ga. Inst. of Technol., Atlanta, 1994.

Ridley, B. A., et al., Measurements and model simulations of the photostationary state during the Mauna Loa Observatory Photochemistry Experiment: Implications for radical concentrations and ozone production and loss rates, *J. Geophys. Res., 97*, 10,375-10,388, 1992.

Ridley, B. A., J. G. Walega, J. E. Dye, and F. E. Grahek, Distribution of NO, NO_x, NO_y, and O_3 to 12 km altitude during the summer monsoon season over New Mexico, *J. Geophys. Res., 99*, 25,519-25,534, 1994.

Ridley, B. A., J. G. Walega, J.-F. Lamarque, F. E. Grahek, M. Trainer, G. Hubler, X. Lin, and F. C. Fehsenfeld, Measurements of reactive nitrogen and ozone to 5 km altitude in June 1990 over the southeastern United States, *J. Geophys. Res., 103*, 8369-8388, 1998.

Roelofs, G.-J., and J. Lelieveld, Distribution and budget of O_3 in the troposphere calculated with a chemistry general circulation model, *J. Geophys. Res., 100*, 20,983-20,998, 1995.

Savoie, D. L., J. M. Prospero, and E. S. Saltzman, Nitrate, non-sea-salt sulfate and methanesulfonate over the Pacific Ocean, in *Chemical Oceanography*, vol. 10, edited by J. P. Riley, R. Chester, and R. A. Duce, pp. 219-250, Academic, San Diego, Calif., 1989.

Shepson, P. B., K. G. Anlauf, J. W. Bottenheim, H. A. Wiebe, N. Gao, and K. Muthuramu, Distribution of reactive nitrogen at a rural site in Ontario during spring 1990 as part of the Eulerian model evaluation field study (EMEFS), paper presented at CHEMRAWN VII, World Conference on the Chemistry of the Atmosphere: Its Impact on Global Change, Baltimore, Md., Dec. 2-6, 1991.

Sillman, S., J. A. Logan, and S. C. Wofsy, The sensitivity of ozone to nitrogen oxides and hydrocarbons in regional ozone episodes, *J. Geophys. Res., 95*, 1837-1852, 1990.

Singh, H. B., and P. L. Hanst, Peroxyacetyl nitrate (PAN) in the unpolluted atmosphere: An important reservoir for nitrogen oxides, *Geophys. Res. Lett., 8*, 941-944, 1981.

Singh, H. B., M. Kanakidou, P. J. Crutzen, and D. J. Jacob, High concentrations and photochemical fate of oxygenated hydrocarbons in the global troposphere, *Nature, 378*, 50-54, 1995.

Singh, H. B., et al., Impact of biomass burning emissions on the composition of the South Atlantic troposphere: Reactive nitrogen and ozone, *J. Geophys. Res., 101*, 24,203-24,220, 1996a.

Singh, H. B., et al., Reactive nitrogen and ozone over the western Pacific: Distribution, partitioning, and sources, *J. Geophys. Res., 101*, 1793-1808, 1996b.

Singh, H. B., et al., Latitudinal distribution of reactive nitrogen in the free troposphere over the Pacific Ocean in late winter/early spring, *J. Geophys. Res., 103*, 28,237-28,246, 1998.

Smyth, S. B., et al., Factors influencing the upper free tropospheric distribution of reactive nitrogen over the South Atlantic during the TRACE A experiment, *J. Geophys. Res., 101*, 24,165-24,186, 1996.

Spivakovsky, C. M., S. C. Wofsy, and M. J. Prather, A numerical method for parameterization of atmospheric chemistry: Computation of tropospheric OH, *J. Geophys. Res., 95*, 18,433-18,440, 1990.

Streets, D. G., and S. T. Waldhoff, Biofuel use in Asia and acidifying emissions, *Energy, 23*, 1029-1042, 1998.

Tabazadeh, A., et al., Nitric acid scavenging by mineral and biomass burning aerosols, *Geophys. Res. Lett., 25*, 4185-4188, 1998.

Talbot, R. W., et al., Chemical characteristics of continental outflow over the tropical South Atlantic Ocean from Brazil and Africa, *J. Geophys. Res., 101*, 24,187-24,202, 1996.

Thompson, A., R. R. Friedl, and H. L. Wesoky, AEAP/SASS (Atmospheric Effects of Aviation Project/Subsonic Assessment), *NASA Ref. Publ., 1385*, Washington, D.C., 1996.

Tiedtke, M., A comprehensive mass flux scheme for cumulus parameterization in large-scale models, *Mon. Weather Rev., 117*, 1779-1800, 1989.

Torres, A. L., and A. M. Thompson, Nitric oxide in the equatorial Pacific boundary layer: SAGA 3 measurements, *J. Geophys. Res., 98*, 16,949-16,954, 1993.

Trainer, M., et al., Observations and modeling of the reactive nitrogen photochemistry at a rural site, *J. Geophys. Res., 96*, 3045-3063, 1991.

U.S. Energy Information Administration (EIA), International Energy Outlook 1997, *Rep. DOE/EIA-0484(97)*, Washington, D.C., 1997.

van Aardenne, J. A., G. R. Carmichael, H. Levy II, D. Streets, and L. Hordijk, Anthropogenic NO_x emissions in Asia in the period 1990-2020, *Atmos. Environ., 33*, 633-646, 1999.

Wang, Y., A. W. DeSilva, G. C. Goldenbaum, and R. R. Dickerson, Nitric oxide production by simulated lightning: Dependence on current, energy, and pressure, *J. Geophys. Res., 103*, 19,149-19,159, 1998a.

Wang, Y., J. A. Logan, and D. J. Jacob, Global simulation of tropospheric O_3-NO_x-hydrocarbon chemistry, 2, Model evaluation and global ozone budget, *J. Geophys. Res., 103*, 10,727-10,755, 1998b.

Weiss, W., A. Sittkus, H. Stockburger, and H. Sartorius, Large-scale atmospheric mixing derived from meridional profiles of Krypton 85, *J. Geophys. Res., 88*, 8574-8578, 1983.

Wildt, J., D. Kley, A. Rockel, P. Rockel, and H. J. Segschneider, Emissions of NO from several higher plant species, *J. Geophys. Res., 102*, 5919-5928, 1997.

Yienger, J., and H. Levy II, Empirical model of global soil-biogenic NO_x emissions, *J. Geophys. Res., 100*, 11,447-11,464, 1995.

P. S. Kasibhatla, Nicholas School of the Environment, Duke University, Durham, NC 27708.

A. A. Klonecki, Advanced Studies Program, NCAR, Boulder, CO 80307.

H. Levy II and W. J. Moxim, NOAA/GFDL, P.O. Box 308, Princeton University, Princeton, NJ 08542. (hl@gfdl.gov)

(Received February 24, 1999, revised June 1, 1999;
accepted June 16, 1999.)